HHS Public Access

Author manuscript

*Cell Metab*. Author manuscript; available in PMC 2022 October 05.

Published in final edited form as:

*Cell Metab*. 2021 October 05; 33(10): 2040–2058.e10. doi:10.1016/j.cmet.2021.09.002.

# Tumor-derived Exosomes Drive Immunosuppressive Macrophages in a Pre-metastatic Niche through Glycolytic Dominant Metabolic Reprogramming

**Samantha M. Morrissey**[1,2], **Fan Zhang**[2,3], **Chuanlin Ding**[2], **Diego Elias Montoya-Durango**[2], **Xiaoling Hu**[2], **Chenghui Yang**[4,5], **Zhen Wang**[4], **Fang Yuan**[6], **Matthew Fox**[7], **Huang-ge Zhang**[1], **Haixun Guo**[8], **David Tieri**[9], **Maiying Kong**[10], **Corey T. Watson**[9], **Robert A. Mitchell**[2], **Xiang Zhang**[6], **Kelly M. McMasters**[2], **Jian Huang**[4], **Jun Yan**[1,2,11,*]

[1]Department of Microbiology and Immunology, University of Louisville School of Medicine, Louisville, KY, USA

[2]Division of Immunotherapy, The Hiram C. Polk, Jr., MD Department of Surgery, Immuno-Oncology Program, Brown Cancer Center, University of Louisville School of Medicine, Louisville, KY, USA

[3]Jiangxi Provincial Children's Hospital, Jiangxi, Nanchang, China

[4]Department of Breast Surgery, Key Laboratory of Tumor Microenvironment and Immune Therapy of Zhejiang Province, Cancer Research Institute of Zhejiang University, The Second Affiliated Hospital, Zhejiang University School of Medicine, Zhejiang, China

[5]Department of Breast Surgery, The First Affiliated Hospital, Wenzhou Medical University, Wenzhou, China

[6]Department of Chemistry, University of Louisville, Louisville, KY, USA

[7]Department of Cardiovascular and Thoracic Surgery, University of Louisville School of Medicine, Louisville, KY, USA

[8]Department of Radiology, University of Louisville School of Medicine, Louisville, KY, USA

[9]Department of Biochemistry and Molecular Genetics, University of Louisville School of Medicine, Louisville, KY, USA

[10]Department of Bioinformatics and Biostatistics, University of Louisville, School of Medicine, Louisville, KY, USA

[*]Correspondence: jun.yan@louisville.edu (J.Y.).

**Author contributions**:

S.M., J.Y., C.D., J.H. conceived this study. S.M., F.Z., C.D., D.E.M., C.Y., Z.W., X.H, H.G., D.T., C.T.W. preformed the experiments and data analysis. F.Y. and X.Z. performed LCFA analysis. M.F., H.Z., R.A.M., K.M.M. contributed the material and reagents. M.K. supervised statistical analyses. S.M. and J.Y. prepared the manuscript. R.A.M., J.H., C.W. K.M.M. revised the manuscript. All authors read and approved the final manuscript.



**Declaration of Interests**:

The authors declare no competing interests.

[11]Lead contact

## Summary

One of the defining characteristics of a pre-metastatic niche, a fundamental requirement for primary tumor metastasis is infiltration of immunosuppressive macrophages. How these macrophages acquire their phenotype remains largely unexplored. Here, we demonstrate that tumor-derived exosomes (TDE) polarize macrophages towards an immunosuppressive phenotype characterized by increased PD-L1 expression through NF-kB-dependent, glycolytic dominant metabolic reprogramming. TDE signaling through TLR2 and NF-κB leads to increased glucose uptake. TDE also stimulate elevated NOS2 which inhibits mitochondrial oxidative phosphorylation resulting in increased conversion of pyruvate to lactate. Lactate feeds back on NF-κB further increasing PD-L1. Analysis of metastasis negative lymph nodes of non-small cell lung cancer patients revealed that macrophage PD-L1 positively correlates with levels of GLUT-1 and vesicle release gene YKT6 from primary tumors. Collectively, our study provides a novel mechanism by which macrophages within a pre-metastatic niche acquire their immunosuppressive phenotype and identifies an important link among exosomes, metabolism, and metastasis.

## Graphical Abstract

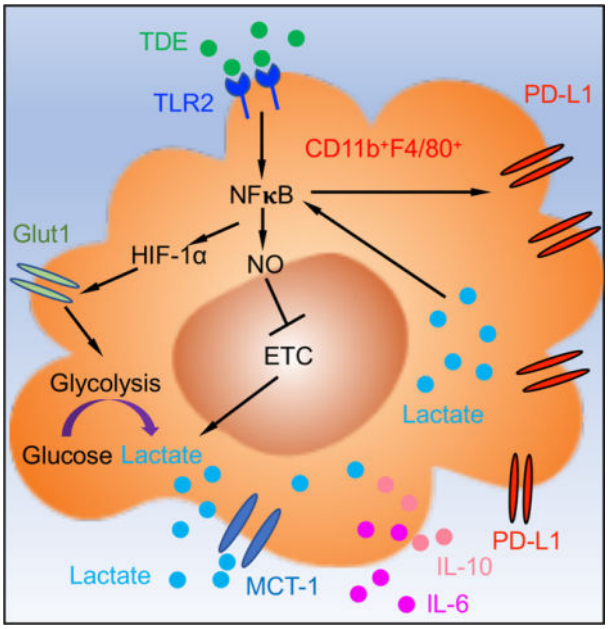


## eTOC Blurb:

Morrissey et al. report that tumor-derived exosomes stimulate pre-metastatic niche macrophages towards an immunosuppressive phenotype through NF-kB dependent, glycolytic dominant metabolic reprogramming, thus promoting tumor metastasis. These pro-metastatic macrophages are characterized by increased *de novo* synthesis of PD-L1 and increased lactate production.

## Introduction

Lung cancer, particularly non-small cell lung cancer (NSCLC), is a common form of cancer worldwide (Herbst et al., 2018). Metastatic lung cancer occurs in 20% to 54% of all solid cancer patients (Seo et al., 2001). Accumulating evidence suggests that cancer metastasis is a temporal and spatial process that starts with the formation of a favorable local environment within a distant tissue. While no cancer cells are present in this future site of metastasis, cancer-associated properties such as immunosuppression, inflammation, and angiogenesis prepare and permit circulating tumor cells to engraft and grow (Liu and Cao, 2016). One of the more notable populations of immune cells within the pre-metastatic niche is the macrophage (Headley et al., 2016). Depletion of macrophages in both breast and colon cancer models significantly decreased the number of metastatic nodules indicating a strong role for macrophages in promoting tumor metastasis (Bader et al., 2018; Linde et al., 2018). However, many questions regarding the mechanisms driving this pre-metastatic macrophage phenotype remain to be elucidated. For example, if macrophages are the major players in the earliest stages of pre-metastatic niche formation; what are the initiating factors and cellular processes driving the immunosuppressive phenotype? Answers to these questions can provide insight into the development of novel therapeutics that reduce the probability of primary tumor metastasis.

One proposed mechanism driving the formation of a pre-metastatic niche is secretion of soluble factors from the primary tumor into systemic circulation. These tumor secreted factors include various cytokines and, more notably, tumor-derived exosomes (TDE) (Binnewies et al., 2018; Liu and Cao, 2016). TDE are small extracellular vesicles that contain snapshots of RNA, DNA, proteins, metabolites, and microRNAs from their parent cells (Kalluri, 2016). TDE often hone to particular highly vascularized tissues like the lung and liver based on their surface integrin profiles (Hoshino et al., 2015). The total concentration of exosomes isolated from the plasma of head and neck squamous cell carcinoma patients positively correlates with active disease status, suggesting a pathogenic nature (Ludwig et al., 2017). Given their abundance and propensity to be found in bodily fluids, exosomes are being targeted clinically as potential biomarkers for cancer (Boukouris and Mathivanan, 2015; Feng et al., 2019).

There has been an increasing focus on how TDE contribute to the complex intracellular communications within the tumor microenvironment (Li and Nabet, 2019). TDE are capable of modulating tumor progression via secretion of pro-inflammatory cytokines, promotion of angiogenesis, TLR-3 driven neutrophil infiltration, and recruitment of myeloid-derived suppressor cells (MDSC) (Bardi et al., 2018; Bretz et al., 2013; Liu et al., 2016; Yang et al., 2018). Exosomal factors including microRNAs have been associated with promoting pre-metastatic niche formation in various cancers (Chin and Wang, 2016). In ovarian cancer, which has one of the highest rates of tumor metastasis within the abdominal cavity, TDE have been shown to induce pre-metastatic niche formation through IL-6 and FasL mediated mechanisms of tumor cell escape (Feng *et al.*, 2019). More recent characterizations in both mice and humans have shown that expression of the immune checkpoint molecule, programmed death ligand-1 (PD-L1), on TDE contributes to systemic immunosuppression, higher overall tumor burdens, and decreased survival in a variety of cancer types (Chen et

al., 2018; Ludwig *et al.*, 2017; Lux et al., 2019; Poggio et al., 2019; Ricklefs et al., 2018). However, how TDE drive PD-L1 expression in a secondary cell type such as macrophages and whether that contributes to pre-metastatic niche formation remains largely unexplored.

In this study, we investigated whether TDE contribute to macrophage mediated pre-metastatic niche formation and if so, by what mechanism. We found that exogenous administration of TDE increased the metastatic burden in the lungs of subcutaneous (s.c.) tumor-bearing mice. Mice treated with TDE have increased expression of PD-L1 on tissue resident interstitial macrophages (IM). TDE increase PD-L1 expression on macrophages through a mechanism dependent on the damage-associated molecular pattern (DAMP), high-mobility group box 1 (HMGB-1) and TLR2. The increased PD-L1 in macrophages results from enhanced *de novo* synthesis, and subsequently curtails immune responses through inhibition of effector T cell functions. In addition, we elucidate a novel mechanistic link between PD-L1 expression and NF-κB dependent glycolytic metabolism. Our findings support the idea that TDE drive pre-metastatic niche formation through NF-κB mediated reshaping of macrophage glycolytic metabolism resulting in an immunosuppressive phenotype.

## Results

### TDE promote tumor metastasis with increased PD-L1 expression on macrophages

Exosomes are known to hone to tissues from their parent cell line of origin (Hoshino *et al.*, 2015). Therefore, we first investigated the role lung cancer derived exosomes play in promoting primary tumor metastasis to the lung. To accomplish this, exosomes were isolated from the murine lung adenocarcinoma cell line, Lewis Lung Carcinoma (LLC) (Thery et al., 2006), and verified by nanoparticle tracking analysis (Figure S1A) (Muhsin-Sharafaldine et al., 2016). Protein array analysis demonstrated expression of known exosome surface markers (Figure S1B). Negative stain electron microscopy showed exosome vesicles in a typical cup-shaped morphology (Figure S1C). Minimal lipoproteins and albumin were detected in the exosome isolates (Figure S1D). Next, we injected non-GFP LLC or control mouse lung epithelial cell (MLE-12) exosomes into C57Bl/6 wild type (WT) mice that 7 days prior had been s.c. injected with LLC-GFP tumor cells (Figure 1A). While mice treated with the MLE-12 exosomes showed no difference compared to untreated tumor-bearing mice, LLC exosome treated mice had an increased number of micro-metastases as assessed by the percentage of LLC-GFP$^+$ cells in the lung (Figure 1B). Fluorescent microscopy analysis confirmed these results (Figure 1C). Further confocal analysis of the lung tissues demonstrated increased PD-L1 co-expression with both CD11b and F4/80 in LLC exosome-treated mice suggesting that the exogenously administered TDE preferentially drive PD-L1 expression on myeloid cells within the lung (Figure 1D).

To examine how specific this result is for lung metastasis, we used exosomes from the mouse pancreatic cancer cell line, Pan02, as an additional control since Pan02 exosomes predominately traffic to the liver (Hoshino *et al.*, 2015). Consistent with previous data, administration of LLC exosomes promoted primary tumor metastasis into the lung while exosomes from Pan02 did not have such effect (Figure 1E). In addition, tumor metastasis predominately occurred in the lung of LLC exosome treated mice but not in the liver

or spleen. We further analyzed PD-L1 expression on lung myeloid cells and found that injection of LLC exosomes, but not Pan02 exosomes, drove upregulated PD-L1 expression on lung IM (Figure 1F). These data further support the specific organotropism of TDE and PD-L1 upregulation in the lungs upon LLC exosome stimulation.

To more definitively examine exosome distribution and cellular uptake, we injected DiI-labeled LLC or MLE-12 exosomes into WT mice. We found that $CD11b^+$ and $CD11c^+$ myeloid cells in the lung had the highest uptake of both MLE-12 and LLC exosomes compared to those cell populations in the spleen and bone marrow (Figure S1E). Although lung $CD11c^+F4/80^+$ alveolar macrophages (AM) had similar uptake levels of MLE-12 and LLC exosomes, lung IM had a significantly higher uptake of LLC exosomes than MLE-12 exosomes (Figure S1E).

Similar to the *in vivo* myeloid phenotype, $F4/80^+$ peritoneal macrophages treated *in vitro* with TDE showed an increase in surface PD-L1 expression as compared with control MLE-12 exosomes or macrophages alone (Figure 1G). These results were confirmed by Western blot analysis (Figure 1H). Confocal analysis of $F4/80^+$ peritoneal macrophages confirmed increased uptake of $GFP^+$ LLC exosomes over time (Figure S1F). Stimulation with exosomes isolated directly from s.c. LLC tumors, which had minimal apoptotic cells (Figure S1G), also demonstrated increased PD-L1 thus eliminating the possibility that the phenotype was an *in vitro* artifact (Figure S1H) (Xiang et al., 2010). The upregulated PD-L1 on macrophages stimulated by TDE was dose dependent (Figure S1I) and TDE stimulation did not induce macrophage death (Figure S1J). TDE stimulation had similar effect on bone marrow-derived macrophages (Figure S1K). *Ex vivo* stimulation of lung macrophages with LLC exosomes showed upregulated PD-L1 expression on lung IM but not on AM (Figure S1L), results consistent with the *in vivo* data. Additionally, to emphasize this phenotype is not only limited to lung cancer, macrophages were treated with exosomes isolated from 4-T1 triple negative breast cancer, MC38 colon cancer, and B16F10 melanoma cell lines all of which demonstrated increased PD-L1 expression (Figure 1I). However, the question remained as to whether exosome stimulation increased endogenous production of PD-L1 by the macrophages or whether the macrophages acquired the PD-L1 passively from the exosomes. Western blot analysis confirmed that LLC and 4T-1 exosomes did express PD-L1, similar to previous reports (Figure S1M) (Chen *et al.*, 2018; Gabrusiewicz et al., 2018; Ricklefs *et al.*, 2018). However, RT-PCR analysis of macrophages treated with LLC exosomes demonstrated a significant increase in PD-L1 mRNA expression and inhibition of RNA transcription by actinomycin D (ACT-D) abrogated this effect (Figure 1J). Further Western blot analysis of macrophages, macrophages stimulated with LLC exosome and LLC exosome alone showed the contribution of exosomal PD-L1 is minimal in the stimulated macrophages (Figure S1N). These results demonstrate that *de novo* synthesis is the main mechanism of increased PD-L1 expression. Taken together, these data suggest that LLC TDE are taken up selectively by $F4/80^+$ macrophages, particularly lung IM, resulting in increased endogenous production of PD-L1, and promote primary tumor metastasis in the lung.

## TDE induce an immunosuppressive phenotype in macrophages

We next explored if TDE stimulation impacts the functionality of macrophages. We first performed a cytokine array on the supernatants from the macrophage culture (Figure 2A). As compared to macrophages alone and macrophages stimulated by MLE-12 exosomes, the TDE stimulated macrophages displayed prominent increases in the secretion of TNF-α, TIMP-1, MCP-1, IL-10, IL-6, IL-1ra, G-CSF, and CXCL1. Notably, all cell supernatants were negative for IFN-γ thus eliminating this as a potential mechanism for PD-L1 upregulation (Zhang et al., 2017). ELISA analysis also confirmed increased IL-6 and IL-10 production (Figure 2B). In addition, LLC exosome stimulation increased mRNA expression levels of arginase-1 (Arg-1) and vascular endothelial growth factor (VEGF) (Figure 2C). However, a dramatic increase in iNOS production supports the emerging notion that macrophages within the tumor microenvironment often display a mixed M1/M2 phenotype (Bardi *et al.*, 2018).

To examine the direct impact of TDE-stimulated macrophages on effector T cell function, we pre-treated macrophages with control MLE-12 or LLC exosomes prior to co-culture with OVA transgenic T cells. As depicted in Figure 2D, $CD8^+$ T cells displayed a dramatic decrease in both cell proliferation and IFN-γ production when co-cultured with TDE-polarized macrophages. This phenotype was largely rescued when neutralizing α-PD-1 was added suggesting that the PD-L1 expression on macrophages is, at least in part, causing functional inhibition of effector T cells. A similar phenotype was seen with $CD4^+$ T cells (Figure S2). These data suggest that TDE stimulation polarizes macrophages towards an immunosuppressive phenotype via direct PD-L1-mediated and indirect cytokine-mediated mechanisms.

## TDE signal through TLR2 and induce NF-kB activation resulting in macrophage upregulation of PD-L1

Toll-like receptors (TLRs) play an important role in innate immunity and are found on sentinel immune cells such as macrophages and dendritic cells (DCs). The increased PD-L1 expression following LLC exosome stimulation was abrogated in TLR adaptor protein MyD88-deficient macrophages (Figure 3A). To identify which specific TLR pathway was involved, peritoneal macrophages from TLR2-, TLR4-, TLR6-, TLR7-, and TLR9-deficient mice were stimulated with TDE. As seen in Figure 3B, the increased PD-L1 expression was only lost in $TLR2^{-/-}$ macrophages, while all other TLR-deficient mice showed enhanced PD-L1 expression similar to WT. Similarly, TNF-α and IL-6 production stimulated by TDE was also abrogated in $TLR2^{-/-}$ mice while other TLR agonists retained their activity (Figure S3A).

To solidify the finding that TLR2 ligation is necessary for exosomes to mediate their effect on macrophages and promote pre-metastatic niche formation, we repeated our initial *in vivo* LLC-GFP s.c. tumor model using $TLR2^{-/-}$ mice. There was no difference in LLC-GFP% in the lungs of the TDE-treated group compared to the controls in $TLR2^{-/-}$ mice (Figure 3C). Furthermore, the LLC-GFP% in the lung of LLC exosome treated mice was significantly reduced in the $TLR2^{-/-}$ mice compared to WT (Figure 3D). Confocal microscopy analysis showed no obvious tumor foci in the lungs of TDE treated $TLR2^{-/-}$

mice (Figure S3B). These results indicate that signaling through TLR2 is required for TDE to mediate upregulated PD-L1 expression on macrophages and influence the progression of primary tumor metastasis to the lung.

Previous studies have linked increased PD-L1 expression to activation of the NF-κB pathway (Asgarova et al., 2018) and TLR2 is well-known to activate the NF-kB pathway. Stimulation with TDE but not control exosomes increased phosphorylation of NF-kBp65 (Figure 3E). In addition, inhibition of NF-κB reduced PD-L1 expression in macrophages (Figure S3C). These results were further confirmed by RT-PCR analysis (Figure 3F). Another prominent signaling pathway previously reported to affect PD-L1 expression is the mechanistic/mammalian target of rapamycin (mTOR) pathway (Lastwika et al., 2016). LLC exosome stimulation of macrophages deficient in the adaptor protein Raptor or Rictor resulted in unaltered levels of PD-L1 expression (Figure S3D), suggesting that this pathway is not involved in this effect.

We next determined which specific exosomal factor activates TLR2. Previous studies have shown that saturated fatty acids can activate TLR2 signaling (Huang et al., 2012; Hwang et al., 2016). We thus performed metabolomics profiling on both MLE-12 and LLC exosomes, focusing on long chain fatty acids (LCFA). LLC exosomes had relatively high abundance of palmitoleic acid, linoleic acid (LA), oleic acid, HODE, and eicosapentaenoic acid (EPA) compared to MLE-12 exosomes (Figure S3E). We next used these LCFA to stimulate macrophages and found that LA, but not other LCFA, could upregulate PD-L1 expression on macrophages although the level was low compared to TDE-stimulated macrophages (Figure S3F).

Another known ligand for TLR2 that has been shown to positively correlate with NSCLC lymph node metastasis is high-mobility group box-1 (HMGB-1) (Wu and Yang, 2018). Overexpression of HMGB-1 has been demonstrated in many types of cancer (Wang et al., 2019; Wu and Yang, 2018; Zhang et al., 2018). LLC whole cell lysate and TDE indicated significant expression of HMGB-1 (Figure S3G). In addition, LLC exosomes expressed more HMGB-1 than MLE-12 exosomes (Figure S3H), although other exosomal markers were differentially expressed. Stimulation of macrophages with recombinant murine (rm)HMGB-1 resulted in increased PD-L1 expression (Figure 3G). Conversely, stimulation of MyD88$^{-/-}$ (Figure 3H) and TLR2$^{-/-}$ (Figure 3I) macrophages with rmHMGB-1 exhibited no change in PD-L1. Exosomes extracted from HMGB-1 knockdown LLC cells substantially reduced their ability to induce PD-L1 expression (Figure 3 J, K). In the orthotopic 4T-1 murine breast cancer model, knockdown of HMGB-1 also decreased overall expression of HMGB-1 in the primary tumor and accordingly decreased the number of metastatic nodules in the lung (Figure 3J). Collectively, these data suggest that tumor-derived exosomal HMGB-1 is the main factor responsible for mediating TLR2 dependent PD-L1 upregulation and subsequent tumor metastasis.

## TDE-induced upregulation of PD-L1 is mediated by metabolic reprogramming

The binary M1/M2 macrophage paradigm previously proposed considers M1 macrophages to be pro-inflammatory, relying on glycolytic metabolism, while M2 are pro-tumor, and oxidative phosphorylation dependent (Jablonski et al., 2015). This dichotomy is now being

challenged by the idea of an overlapping macrophage spectrum with cells capable of exhibiting both anti-tumoral and pro-tumoral characteristics depending on environmental context and stage of tumor progression (Jeong et al., 2019; Sica and Mantovani, 2012). To first explore if metabolic alterations drive TDE-mediated macrophage polarization, glucose-deprived macrophages were co-cultured with 2-NBDG to assay glucose consumption. TDE-stimulated macrophages had significantly increased glucose uptake over control macrophages (Figure 4A). Addition of the glycolysis inhibitor, 2-deoxyglucose (2-DG) significantly downregulated PD-L1 expression following TDE stimulation suggesting a role for glycolysis in driving PD-L1 expression (Figure 4B). Further analysis of metabolic enzymes showed increases in glucose transporter-1 (GLUT-1), hypoxia inducible factor-1α (HIF1-α), and lactose dehydrogenase A (LDHA) expression (Figure 4C). Pyruvate dehydrogenase kinase 1 (PDK1) was increased in both of the exosome-stimulated groups and hexokinase-1 (HK1) demonstrated no considerable differences between TDE and controls. These results were confirmed using western blot analysis (Figure 4D).

Increased glucose uptake coupled to increased GLUT-1, HIF-1α, and LDHA expression suggest that TDE stimulated macrophages favor a highly glycolytic metabolic profile despite being in normoxic conditions. To confirm this hypothesis, we performed a series of Seahorse assays to assess glycolytic and mitochondrial function. Using a glycolytic stress assay, macrophages showed increased extracellular acidification rate (ECAR) in the LLC exosome treated group as compared to controls (Figure 4E). Analysis of the oxygen consumption rate (OCR) showed that TDE-stimulated macrophages were unresponsive to mitochondrial inhibitors, oligomycin and FCCP (Figure 4F). This effect was not due to an excessive TDE treatment (Figure S4A). The associated bioenergetic profile showed a high level of non-mitochondrial oxygen consumption in the TDE treated macrophages signifying that another mechanism outside of mitochondrial ATP generation utilized the oxygen (Figure 4G). DCFDA staining showed TDE-stimulated macrophages generated less reactive oxygen species (ROS) than the two control groups eliminating this as the potential source of oxygen consumption (Figure S4B). Another molecule often found within the tumor microenvironment that utilizes oxygen is nitric oxide (NO) (Salimian Rizi et al., 2017). In addition to consuming free oxygen, NO can inhibit the electron transport chain via interfering with proper functioning of complexes III and IV within actively respiring mitochondria (Figure S4C) (Everts et al., 2012). We found that TDE stimulation increased intracellular NOS2 expression (Figure 4H), which agrees with the previously shown mRNA iNOS data (Figure 2C). Addition of the NOS2 inhibitor, S-ethylisothiourea hydrobromide (SEITU) completely rescued the oxidative respiration capacity of the macrophages while decreasing the glycolytic capacity and ECAR (Figure 4I). The bioenergetic profile demonstrated properly restored ATP synthesis in a dose dependent manner (Figure S4D). Furthermore, stimulation of macrophages with TDE in the presence of SEITU decreased PD-L1 expression (Figure 4J), suggesting that the PD-L1 levels induced by TDE are positively associated with glycolytic metabolism but negatively associated with oxidative pathway. NOS2 expression in TDE stimulated macrophages was dependent on MyD88 signaling (Figure 4K) but independent of HIF1-α (Figure 4L) indicating that NOS2 and HIF-1α influence glycolysis through two separate mechanisms. To further examine the *in vivo* role of NOS2 on premetastatic niche macrophages and subsequent tumor metastasis,

NOS2$^{-/-}$ mice were injected with LLC exosomes and lung tumor metastasis was monitored. WT and NOS2$^{-/-}$ mice had comparable primary tumor burdens (data not shown). WT mice injected with LLC exosomes had higher tumor metastasis in the lungs compared to control WT mice (Figure 4M), consistent with our previous result (Figure 1). However, this difference was not observed in NOS2$^{-/-}$ mice. Examining lung macrophages, lung IM had increased PD-L1 expression in WT mice injected with LLC exosomes but not in NOS2$^{-/-}$ mice (Figure 4N). This *in vivo* data highlights a role for NOS2 in cancer metastasis and further supports our *in vitro* data that TDE induce PD-L1 upregulation in part through NOS2-mediated inhibition of oxidative metabolism.

Further investigation into HIF-1α's role in TDE metabolic reprogramming revealed that TDE-induced upregulation of GLUT-1 mRNA expression was abolished in HIF-1α$^{-/-}$ macrophages. PD-L1 expression following TDE stimulation was also significantly decreased (Figure S5A). In addition, TDE stimulated upregulation of HIF-1α and GLUT-1 was abrogated in MyD88$^{-/-}$ macrophages, indicating that these factors are indeed downstream of TLR2 signaling and are mediated by exosomal ligation (Figure S5B). Interestingly, inhibition of NF-κB also decreased TDE-stimulated HIF-1α expression suggesting HIF-1α activation lies downstream of NF-κB (Figure S5C). Using LLC-GFP s.c. tumor model, we investigated the role HIF-1α plays on mediating PD-L1 expression in a pre-metastatic niche. Our results showed a blunted PD-L1 response to LLC exosome treatment in lung IMs from HIF-1α cKO mice as compared to control (Figure S5D). These data support our *in vitro* finding, suggesting that HIF-1α plays a secondary role to NOS2 in driving PD-L1 expression.

Collectively, our data demonstrate that TDE polarize macrophages through metabolic reprogramming to increase PD-L1 expression. Specifically, NF-κB is the master transcription factor that utilizes HIF-1α/GLUT-1 to bring more glucose into macrophages and NOS2/NO to inhibit mitochondrial oxidative phosphorylation. Stimulation with the oxidative metabolite, α-ketoglutarate, abrogated the increase of PD-L1 expression in TDE stimulated macrophages (Figure S5E), further strengthening the association between glycolysis and PD-L1 expression.

## TDE induced lactate production drives PD-L1 expression through NF-κB

One of the classic hallmarks of Warburg metabolism is not only glycolysis in normoxic conditions but also the shunting of pyruvate away from Acetyl-CoA into lactate. Having demonstrated that TDE polarize macrophages towards a highly glycolytic phenotype, we hypothesized that lactate production may be enhanced in TDE-treated macrophages and lactate may act as a critical metabolite to induce PD-L1 expression. Measuring the concentration of lactate in the supernatants from TDE-stimulated macrophage culture showed augmented lactate secretion (Figure 5A). Increasing numbers of macrophages increased the concentration of secreted lactate (Figure S5F). The increased lactate was a result of exosomal ligation and signaling through the MyD-88 (Figure 5B) and NF-kB pathways (Figure 5C). The amount of secreted lactate was notably reduced in HIF-1α$^{-/-}$ macrophages but not back to baseline, again providing evidence for the contribution of the NOS2 pathway to lactate secretion (Figure 5D). The mRNA expression of lactate

exporter, monocarboxylate transporter-4 (MCT4) was also increased, which may account for increased ability of these cells to secrete lactate into the supernatant (Figure 5E).

We next sought to determine if lactate was the ultimate downstream metabolite of augmented glycolysis that was responsible for driving increased PD-L1 expression. Stimulation of macrophages with lactate increased PD-L1 expression (Figure 5F). Specific inhibition of lactate transporter MCT-1 by AZD3965 negated lactate-induced PD-L1 upregulation (Figure 5G). Furthermore, Phosflow assay revealed that lactate induced phosphorylation of NF-κBp65 at 15 and 30-minutes (Figure 5H). These results were verified using a confocal microscopy which demonstrated peak NF-kBp65 translocation into the nucleus at 30 minutes following lactate stimulation and regression to the cytoplasm by one hour (Figure 5I). Flow cytometric analysis further confirmed lactate induced PD-L1 expression in an NF-κB-dependent manner (Figure 5J). RT-PCR results recapitulated this finding (Figure 5K). RT-PCR analysis also showed an increase in lactate importer MCT-1 following TDE stimulation suggesting extracellular as well as intracellular lactate can drive this phenotype (Figure S5G).

Together, these data show a novel role for lactate in driving PD-L1 expression. Specifically, we propose in our model that TDE signaling activates NF-κB and its downstream effectors NOS2 and HIF-1α, to augment glycolytic metabolism and shunt pyruvate into lactate (Figure 5L). The newly synthesized lactate is able to feedback on NF-κB, further increasing PD-L1 expression and maintaining the enhanced glycolytic phenotype.

### The effect of TDE on *in vivo* pre-metastatic niche formation

Next, we wanted to confirm that tissue resident macrophages *in vivo* also display this augmented glycolytic phenotype following TDE stimulation. To achieve this, we injected WT mice with LLC or MLE-12 exosomes every 3 days for 2 weeks (Figure 6A). The day after the final treatment, mice were i.p. injected with $^{18}$F-fluorodeoxyglucose (FDG). Clinically, $^{18}$F-FDG positron emission tomography/computed tomography is an essential imaging modality for NSCLC lesions with increased uptake often correlating with increased tumor PD-L1 expression (Takada et al., 2019). In our study, one hour after injection of $^{18}$F-FDG, the mice were euthanized and whole lung radioactivity was measured which demonstrated no significant difference between the two treatment groups (Figure 6B). However, the macrophage enriched population isolated from the lungs of TDE treated mice had a marked increase in $^{18}$F-FDG uptake (Figure 6C). Furthermore, the macrophage enriched population from the TDE group also demonstrated increased expression of PD-L1, HIF-1α, and MCT-4, as compared to the control group (Figure 6D). These results validate our *in vitro* findings that TDE stimulation results in enhanced glycolytic metabolic reprogramming of tissue resident macrophages which drives upregulation of PD-L1.

We next examined how the TDE driven phenotype impacts the immune landscaping of a pre-metastatic niche *in vivo*. H&E staining confirmed the lungs were negative for overt primary tumor metastasis at end point (Figure S6A). Analysis of the IM and AM populations (Figure S6B) showed that the IM population dramatically increased in the tumor-bearing mice while the AM remained largely unchanged compared to the control. Furthermore, the IM demonstrated increased PD-L1 expression within this pre-metastatic tumor environment

whereas the AM showed no change (Figure S6B). Other noticeable effects within the lung included a decrease in monocytes and an increase in MDSCs in tumor-bearing mice (Figure S6C).

Next, we aimed to demonstrate that TDE, specifically, are responsible for mediating the increased PD-L1 expression in the IM compartment allowing for priming of lung cancer metastasis. To address this question, we used CRISPR/CAS-9 technology to edit RAB27a, a critical regulatory protein necessary for exosome secretion, in the 4T-1 breast carcinoma cells (van Niel et al., 2018). Given that breast cancer, particularly triple-negative breast cancer, often metastasizes to the lungs, a triple negative primary 4T-1 orthotopic breast cancer with metastasis to the lung served as a clinically relevant model. Western blot analysis showed about a 50% reduction in Rab27a expression following transfection (Figure S6D). There was no difference in overall primary tumor burden between the scrambled (SCRAM) control and the Rab27$^{-/-}$ cells (Figure 6E). However, the lung resident CCR2$^{-}$ IM population that expanded the most in the exosome competent tumor was significantly diminished in RAB27$^{-/-}$ tumors (Figure 6F). Moreover, RAB27 knockdown decreased PD-L1 expression in the CCR2$^{-}$ IM compartment and left the CCR2$^{+}$ unchanged (Figure 6G). The AM compartment displayed no change following RAB27 depletion (Figure S6E). These data suggest that TDE specifically impact the tissue resident IM to drive PD-L1 expression in the pre-metastatic niche.

The collective immune landscape in the lung following RAB27 depletion demonstrated an overall more active immune profile. There was a decrease in the percentage of MDSCs (Figure S6F) and analysis of the T-cell compartment within the lung demonstrated an increase in percentage of CD8$^{+}$ T cells (Figure 6H) with a trending decrease in PD-1 expression (Figure S6G). Conversely, the overall percentage of CD4$^{+}$ T cells in the Rab27$^{-/-}$ tumor-bearing mice was unchanged (Figure 6I) but there was a significant decrease in PD-1 expression (Figure 6J). These results together indicate that circulating exosomes from primary tumors are capable of trafficking into the lung and increasing the expression of PD-L1 on the tissue resident IM, inducing an increased in PD-1$^{+}$ T cells and recruiting MDSCs to the pre-metastatic site.

## Human NSCLC exosomes alter CD14$^{+}$ macrophage metabolism and prime LN for metastasis

To ascertain the clinical relevance of our findings, we sought to recapitulate the phenotype using exosomes derived from human tumor cells. As shown in Figure 7A, exosomes isolated from the human NSCLC A549 cell line but not the control human bronchial epithelial cell line (HBEC) increased PD-L1 expression on CD14$^{+}$ monocytes. Exosomes from human breast carcinoma MCF7 and pancreatic ductal adenocarcinoma (PDAC) S2-013 cell lines had a similar effect (Figure 7B). Co-culture of TDE treated CD14$^{+}$ cells with autologous CD3$^{+}$ T cells demonstrated that A549 TDE polarized CD14$^{+}$ cells drastically inhibited both CD4 and CD8 T cell proliferation as well as IFN-γ production from CD8$^{+}$ T cells (Figure S7A). Stimulation with recombinant human HMGB-1 increased PD-L1 expression in CD14$^{+}$ cells (Figure S7B). Addition of TLR2-blocking antibody decreased PD-L1 expression indicating human TDE also signal through TLR2 to drive PD-L1 expression

(Figure S7C). Inhibition of NF-κB also decreased PD-L1 expression on TDE stimulated $CD14^+$ cells (Figure S7D).

Investigation into metabolic alterations demonstrated that inhibition of glycolysis via 2-DG decreased PD-L1 expression following A549 exosome treatment (Figure S7E). Flow cytometric analysis of GLUT-1 showed increased expression following TDE stimulation (Figure S7F). We found that lactate secretion was dependent on TLR2 signaling (Figure S7G). Likewise, stimulation with exogenous lactate increased PD-L1 expression through NF-κB pathway (Figure S7H). Overall, these data suggest that human TDE metabolically reprogram $CD14^+$ monocytes via the same metabolic mechanism elucidated in mouse models.

To further examine how our pre-clinical model could correlate with clinical outcomes, we obtained draining lymph node (dLN) samples from NSCLC patients that were negative for tumor cell infiltration to best mimic a pre-metastatic niche (Supplemental Table 1). We compared those LNs to the LNs from lung transplant donors, which were considered to be healthy donors in this case. Overall analysis of surface marker expression within the myeloid cell compartment indicated increased levels of $CD16^+$, $CD33^+$, $CD63^+$, $CD68^+$, and $CD206^+$, suggesting an overall activated, classic M2 phenotype in cells from patient samples (Figure S7I). Furthermore, when specifically looking at CD206 and PD-L1 co-expression in the $CD68^+$ macrophages, there was roughly double the expression in the NSCLC cohort compared to healthy controls (Figure 7C). DCs within the NSCLC dLN also expressed PD-L1 although $CD206^+$ macrophages had the highest percentage of PD-L1 expression (Figure 7D). Notably, macrophage CD206/PD-L1 co-expression positively correlated with PD-1 expression on the $CD8^+$ T cells within the dLN (Figure 7E). Taking the immune phenotype markers together, principal component analysis (PCA) of the myeloid and T cell populations within the LNs demonstrated a significant difference in mean expression pattern between NSCLC patients and healthy donors (Figure 7F).

We next investigated whether macrophages within the dLN undergo similar metabolic reprogramming. We split the $CD68^+$ macrophages into two groups, $CD206^{hi}PD\text{-}L1^{hi}$ and $CD206^{lo}PD\text{-}L1^{lo}$, and then measured GLUT-1 expression. The $CD206^{hi}PD\text{-}L1^{hi}$ group demonstrated an increased GLUT-1 expression compared to the $CD206^{lo}PD\text{-}L1^{lo}$ (Figure 7G). Strikingly, given the small sample size, the GLUT-1 expression on the $CD68^+$ cells positively correlated with their CD206/PD-L1 expression (Figure 7H). Taken together, these results suggest that despite the negative LN staging, dynamic changes in the local myeloid and T cell populations have already been made, possibly readying the tissue for metastatic tumor cell arrival. However, the question remained whether these immunological and metabolic changes within the dLN were associated with an exosomal phenotype from the primary tumor.

To address this question, we turned to the TCGA dataset to see if we could find a correlation between exosome release genes and nodal metastasis. We divided patients into two groups based on nodal staging, NX/N0 were considered negative whereas N1-N3 were considered positive for metastasis. Our screening revealed that two exosome release genes, YKT6 (Figure 7I) and TSG101 (Figure S7J), had higher expression in the primary tumor of lung

adenocarcinoma patients with positive nodal metastasis compared to nodal negative. A similar phenotype for YKT6 was also seen in patients with colon adenocarcinoma (Figure S7K). The top quartile of lung adenocarcinoma patients expressing YKT6 demonstrated significantly poorer survival outcomes when compared to the bottom quartile (Figure 7J). To further confirm that YKT6 gene expression is correlated with exosome release, we transfected A549 lung cancer cells with GFP tagged YKT6 gene plasmid or GFP alone plasmid. Transfected A549 cells exhibited similar intensity of green fluorescence (Figure S7L). Western blot analysis showed that A549 cells transfected with GFP-YKT6 plasmid expressed GFP-YKT6 fusion protein (Figure S7M). Interestingly, the endogenous YKT6 level was also increased. We then extracted exosomes from those transfected cells. Nanoparticle tracking analysis indicated that A549 transfected with GFP-YKT6 secreted approximately 5-fold more exosomes than those from cells transfected with GFP alone (Figure S7N).

Turning to our own NSCLC patient cohort, we found that $CD45^{-}$ tumor cells displayed increased expression of YKT6 (Figure 7K) and TSG101 (Figure S7O) as compared to $CD45^{+}$ cells sorted from primary tumor. Furthermore, there was a trending positive correlation between YKT6 expression in the primary tumor cells and PD-L1 expression in the dLN (Figure S7P). TSG101 also showed a trending positive correlation (Figure S7Q). Grouping the NSCLC patients into cohorts based on their nodal PD-L1 expression level (high >10% $CD68^{+}CD206^{+}PD\text{-}L^{+}$ and low <10% $CD68^{+}CD206^{+}PD\text{-}L^{+}$ expression), demonstrated a significantly increased primary tumor YKT6 mRNA level in the $PD\text{-}L1^{high}$ cohort over the $PD\text{-}L1^{low}$ (Figure 7L). These results suggest at least a positive association in our NSCLC patient cohort between release of primary tumor-derived exosomes and the immunosuppressive landscape of the myeloid and T cells in the dLN.

## Discussion

Immune checkpoint blockade (ICB) therapy using either PD-1 or PD-L1 antibodies has demonstrated significant clinical benefit in NSCLC (Borghaei et al., 2015). While it was originally thought tumor cells were the main source of PD-L1-mediated suppression, recent studies have indicated that PD-L1 expression on DCs or macrophages play a more dominant role in determining efficacy of PD-1 ICB therapy (Lin et al., 2018; Tang et al., 2018). Given the importance of PD-L1 on myeloid cells, it is paramount to determine what drives expression of PD-L1. PD-L1 expression on exosomes themselves has been credited to induce an overall immunosuppressed phenotype (Chen *et al.*, 2018). Furthermore, PD-L1 expression on plasma exosomes but not soluble PD-L1 has been shown to positively correlate with disease activity and clinical stage in head and neck squamous cell carcinoma patients suggesting a causative role in disease progression (Theodoraki et al., 2018). In our study, elimination of exosome secretion from the primary tumor decreased expression of PD-L1 on lung resident $CCR2^{-}$ IM and decreased recruitment of MDSCs, while increasing effector T cell infiltration. *In vitro* analysis demonstrated that TDE increased the *de novo* synthesis of PD-L1 in macrophages. We conclude that PD-L1 expression on macrophages induced by TDE is not dependent on exosomal PD-L1 transfer. Several lines of evidence support this conclusion including 1) minimal PD-L1 shown in exosomes by Western blot analysis where the same concentration of exosomes was used for macrophage stimulation,

2) increased PD-L1 mRNA levels, 3) a dependence on TLR2 and MyD88 signaling, and 4) perturbations in glycolytic metabolism that dramatically affect PD-L1 expression. In an attempt to determine what exosome associated factor(s) elicits the TLR2 activation, we assayed for the effect of LCFA and HMGB-1 on driving PD-L1 expression. LA at 25μM stimulated upregulation of PD-L1 expression on macrophages. UVB radiation of melanoma cells previously has been shown to increase their expression of PD-L1 in an HMGB-1 dependent manner via RAGE pathway (Wang *et al.*, 2019). HMGB-1 also signals through TLR2/TLR4 for its activity (Aucott et al., 2018; Yu et al., 2006). Here we demonstrate that exosomal HMGB-1 signals through TLR2 to stimulate PD-L1 expression on myeloid cells in both mice and humans. The differences may lie in the sources of HMGB-1. Extracellular HMGB-1 preferentially activates TLR2/4/RAGE pathway (Aucott *et al.*, 2018). Therefore, as LA abundance in LLC exosomes is relatively low, exosomal HMGB-1 may play a more dominant role. Indeed, exosomes extracted from HMGB-1 knockdown tumor cells abolished their ability to induce PD-L1 upregulation. In addition, elimination of HMGB1 in primary s.c. tumors decreased the number of metastatic lesions in the lung pointing towards a causative role in tumor metastasis further supports this notion. It is worth noting that other TLRs including TLR4 and TLR7 have been shown to be involved in melanoma extracellular vesicles mediated upregulation of PD-L1 on mouse immature myeloid cells (Fleming et al., 2019). TDE from chronic lymphocytic leukemia also stimulate PD-L1 expression on monocytes via TLR7 signaling (Haderk et al., 2017). Although exosomes do contain RNA, the exosomal RNA did not stimulate macrophage PD-L1 upregulation in our study. This may be due to the relative low concentrations of RNA in TDE. It is also possible that TDE from different cancer types may contain variable levels of RNAs.

Within the pre-metastatic niche, macrophages are often classified as the tumor-promoting, “M2” subtype, indicated by their increased Arg-1 expression and reliance on mitochondrial oxidative metabolism. This paradigm was recently challenged when human monocytes were cultured with conditioned media from PDAC and demonstrated a pronounced glycolytic signature reminiscent of the Warburg effect (Penny et al., 2016). The increased rate of glycolysis in tumor cells ultimately drives an increased production of lactate, a pro-tumoral metabolite capable of increasing KRAS driven tumor growth and reducing anti-tumor T cell expansion (Colegio et al., 2014; Fischer et al., 2007). Recently, intracellular lactate was found to induce a new type of epigenetic modification called lactylation that drove M2 gene expression within a classic M1 polarized macrophage (Zhang et al., 2019). Here, we demonstrate another novel mechanism by which macrophages acquire a “non-classical M1” phenotype characterized by PD-L1 mediated immunosuppression and enhanced glycolytic metabolism. While lactate has previously been associated with an immunosuppressive TAM phenotype (Colegio *et al.*, 2014), we discover a role for lactate in driving PD-L1 expression in an autocrine manner. Any inhibitory perturbations to our proposed glycolytic pathway significantly decreased PD-L1 expression due to blunted lactate production. Furthermore, addition of an oxidative metabolite like α-ketoglutarate blocked TDE driven PD-L1 upregulation again strengthening the important relationship between glycolysis, lactate and PD-L1.

We demonstrate that the NF-kB pathway directly regulates this “non-classical M1” phenotype. In addition to directly facilitating PD-L1 expression by binding to the promoter

(Asgarova *et al.*, 2018), we report here a novel mechanism by which NF-κB regulates PD-L1 expression through metabolic alterations. Following signaling from TLR2/MyD88 TDE ligation, NF-κB activates two distinct pathways that independently augment glycolysis. First, HIF-1α activation leads to an increased expression of GLUT-1 resulting in a higher rate of influx of glucose into macrophages. Secondly, activated NOS2 increases the production of NO which in turn inhibits complexes III and IV of the electron transport chain thus shunting pyruvate into lactate (Figure 5L). Blockade of NO by SEITU restored normal oxidative metabolism further supporting the notion of a Warburg-like phenotype. This mechanism is supported by both *in vitro* data and *in vivo* studies using $NOS2^{-/-}$ mice and HIF-1α myeloid cell-specific deletion mice. We further demonstrate that exogenous lactate directly activates NF-kB leading to PD-L1 expression on macrophages. Addition of MCT-1 inhibitor AZ3965 reduced lactate-induced PD-L1 expression on macrophages indicating uptake of lactate intracellularly is necessary to drive PD-L1 expression. However, lactate is not packaged in LLC exosomes through our metabolomics profiling, suggesting lactate is mainly produced by TDE-induced glycolysis. Interestingly, previous studies have shown that lactate stimulates NF-kB activation in endothelial cells (Vegran et al., 2011) and cancer-associated fibroblasts (Apicella et al., 2018) to drive tumor angiogenesis and adaptive resistance to targeted therapies.

In an effort to determine if exosomes contribute to pre-metastatic niche formation in human cancer patients, we used dLN samples from cadaveric lung transplant organs as healthy controls and compared them to dLN from NSCLC patients. We chose dLN samples from patients with T1N0-T3N0 staging which by current practices in staging should be negative for tumor cell infiltration and could best mimic a pre-metastatic niche in humans (Silvestri et al., 2013). The patient dLN displayed an already increased proportion of $CD206^{+}PD\text{-}L1^{+}$ macrophages, particularly for some patients. Furthermore, the expression of PD-L1 on these macrophages positively correlated with surface GLUT-1 expression which seemingly suggests that the PD-L1 expression could stem, in part, from an increased glycolytic capacity. These findings point towards an altered immune profile despite negative nodal staging.

To demonstrate a link between nodal metastasis and exosomes from primary tumors, we found that out of the 20 known exosome release genes, two in particular, YKT6 and TSG101 correlated with positive metastatic nodal staging in the LUAD patient cohort within the TCGA database (Hessvik and Llorente, 2018). We were able to substantiate this data using dLN and primary tumor samples from our own NSCLC patient cohort. Specifically, there was a trending correlation between YKT6 expression in the primary tumor cells and PD-L1 expression on macrophages in the dLN. The lack of significance is most likely due to the limited size of the patient samples. Nevertheless, grouping the 8 patients into cohorts based on their PD-L1 expression level (high >10% $CD68^{+}CD206^{+}PD\text{-}L^{+}$ and low <10% $CD68^{+}CD206^{+}PD\text{-}L^{+}$ expression), YKT6 mRNA levels were significantly increased in the high cohort over the low. Collectively, these results suggest that primary tumors capable of secreting high amounts of TDE have an increased likelihood of metastasis due to the ability of TDE to reprogram the immune landscape within the pre-metastatic site towards an immunosuppressive $PD\text{-}L1^{+}$ phenotype on macrophages.

A recent study profiling immune activation and evasion throughout the developmental stages of carcinogenesis in human lung squamous cell carcinoma found an increased abundance of M1 macrophages in high grade lesions and early carcinoma as compared to low grade lesions clearly demonstrating the M1 phenotype is not solely pro-inflammatory in nature but could be pro-carcinogenic as well (Mascaux et al., 2019). Further analysis of these high-grade lesions showed enrichment for PD-L1, IL-10, and IL-6, an immunomodulatory profile that bears a striking resemblance to our TDE-stimulated “non-classical M1” macrophages. Additional studies in early stage lung cancer have also shown that M1 macrophages exhibit the highest expression level of PD-L1 compared to TAM and classical M2 (Singhal et al., 2019). Collectively, these data emphasize the potential clinical relevance of our study. The presence of PD-L1$^{+}$, “non-classical M1” macrophages along with other tumor promoting characteristics could be used as an immune biomarker to indicate early primary carcinogenesis or, as we propose, pre-metastatic niche formation. It is also important to consider the potential of targeting pathogenic exosomal release genes like YKT6. NSCLC patients with high YKT6 expression have previously been shown to have increased plasma concentrations of exosomes and worse survival outcomes (Ruiz-Martinez et al., 2016). We demonstrated that overexpression of YKT6 in A549 increases overall exosome secretion. Within our own NSCLC patient cohort, YKT6 was shown to be increased in primary tumors and positively correlated with an immunosuppressive phenotype within the dLN.

In summary, we discovered that TDE polarize tissue-resident macrophages towards an immunosuppressive phenotype in a pre-metastatic niche through metabolic reprogramming. This effect is regulated by NF-κB mediated augmentation of glycolysis and subsequent generation of lactate. This immunosuppressive “non-classical M1” phenotype is characterized by: 1) increased *de novo* synthesis of PD-L1, 2) increased glucose uptake and GLUT-1 expression, and 3) increased conversion of pyruvate into lactate with subsequent lactate driven PD-L1 expression. Our findings provide novel insight into how TDE orchestrate a pro-metastatic phenotype by metabolically reprogramming tissue resident macrophages.

### Limitations of Study

While we included dLN samples from human NSCLC patients to validate macrophage metabolic reprogramming within a premetastatic niche mediated by TDE, the overall sample size was small. We have not studied whether lactate level within dLN interstitium is associated with CD206$^{+}$PD-L1$^{+}$ macrophages.

## STAR METHODS:

### RESOURCE AVAILABILITY:

**Lead contact—**Further information and request for resources and reagents should be directed to and will be fulfilled by the lead contact, Jun Yan (jun.yan@louisville.edu).

**Material availability—**This study did not generate any new unique reagents.

### Data and code availability

- All raw data including western blots are available from the lead contact upon request.
- This paper does not report original code.
- Any additional information required to reanalyze the data reported in this paper is available from the lead contact upon request.

## EXPERIMENTAL MODEL AND SUBJECT DETAILS

**Human Samples—**Human samples were obtained as approved by the University of Louisville Institutional Review Board. Written informed consent was obtained from either subjects or their legal authorized representatives prior to sample collection. Draining LNs were obtained from lung transplant donors during lung resection and from cancer patients during tumor resection and/or biopsy. Patient information was summarized in Table S1. Patient ages ranged from 57 to 69 (4 males and 5 females). PBMCs were obtained from healthy donors. Healthy donor ages ranged from 28–57 (14 males and 3 females). The influence of association of sex, gender or both on the results of the study could not be performed due to insufficient statistical power. The human LNs were smashed with 5 ml syringe column (BD) and then filtered through 40μm cell strainer (VWR North American) to make a single cell suspension. LN cells were washed with RPMI 1640 and then frozen in −140 °C freezer (2–3 million cells per vial) until future use. The human LN samples were stained with conjugated antibodies (Key Reference Table) and ran on either a BD FACS Canto or a Helios CyTOF (Fluidigm).

**Human PBMC Isolation—**Whole blood samples were centrifuged at 1600 rpm for 10 min. Plasma was aspirated and aliquoted into 1mL Eppendorf tubes and immediately stored at −80°C until future use. The remaining cell layers were diluted with an equal volume of complete RPMI1640. The blood suspension was layered over 5mL of Ficoll-Paque (Cedarlane Labs, Burlington, ON) in a 15mL conical tube. Samples were then centrifuged at 2,000 rpm for 30 min at room temperature (RT) without brake. The mononuclear cell layer was then transferred to a new 15mL conical tubes and washed with complete RPMI 1640. The cell pellet was resuspended in 3mL of RPMI1640 and counted for sample processing.

**Mice—**C57BL/6, BALB/cJ, MyD88$^{-/-}$, TLR2$^{-/-}$, TLR4$^{-/-}$, TLR6$^{-/-}$ TLR7$^{-/-}$, iNOS$^{-/-}$, OT-I and OT-II mice were purchased from commercially available vendors (key Resources Table). All genetically deficient mice and OT-1 and OT-II mice were on C57BL/6 background. TLR9$^{-/-}$ mice were purchased from Oriental Yeast Co. (Japan). All purchased animals used for experiments were age (6–8 weeks) and sex matched. For WT mouse only studies, mice were used directly importing into the facility. For WT and KO mouse studies, the in-house mating mice were used. LysM-cre;HIF1-α$^{fl/fl}$ mice were generated by crossing LysM$^{Cre/wt}$ and HIF-1α $^{f/f}$ mice both which were purchased from Jackson Laboratory (Bar Harbor, ME). LysM-cre;Raptor$^{fl/fl}$ and LysM-cre;Rictor$^{fl/fl}$ mice were generated in a similar manner. Homebred littermates of the same sex were randomly assigned to experimental groups. Both male and female mice were used. Mice were maintained on a 12-hour dark/light cycle at room temperature. The standard laboratory autoclavable rodent

diet (5010, LabDiet) were used to feed mice. All animals were housed in barrier facility and only healthy mice were used for experiments. Sentinel animals were tested for CAR bacillus, Encephalitozoon cuniculi, Ectromelia, EDIM, LCMV, Mycoplasma pulmonis, MAV1, MAV2, MCMV, MHV, MNV, MPV, MVM, Polyoma, PVM, REO3, TMEV, Sendai, Clostridium piliforme by serology and PCR testing for fur mites and pin worms. Testing was performed by IDEXX Laboratories. All animals in this room and the facility consistently test negative SPF from 2017-present. Mice were treated in accordance with institutional guidelines and approved by the Institutional Animal Care and Use Committee at the University of Louisville, Louisville, KY.

**Cell culture and cell lines—**The authenticated human lung adenocarcinoma cell line A549, human breast adenocarcinoma cell line MCF7, murine lung adenocarcinoma (LLC), colon carcinoma (MC38), and melanoma (B16-F10) cell lines were obtained from American Type Culture Collection (ATCC). The murine breast cancer cell line 4T-1 was kindly provided by Dr. Nejat Egilmez, Department of Microbiology and Immunology, University of Louisville. The control MLE-12 cell line was provided by Dr. Haribabu Bodduluri, the human HBEC cell line provided by Dr. Geoffrey Clark, and the human S2-013 human pancreatic cell line was provided by Dr. Robert Martin. The Pan02 cell line was provided by Dr. Yong Lu at Wake Forest University. All cell lines were cultured at 37°C with 5% $CO_2$ in DMEM supplemented with 10% FBS (Atlanta Biologicals), and 1% Penicillin-Streptomycin Solution (Corning). For exosome isolation studies, cells were cultured in appropriate medium with 10% exosome-free FBS (Thermo-Fisher Scientific, Waltham, MA). All cell lines were routinely tested for the presence of mycoplasma using the universal mycoplasma detection kit (ATCC, Manassas, VA).

## METHOD DETAILS

**CRISPR/CAS9 RAB27 knockdown cell line—**RAB27KO 4T-1 cell line was generated using CRISPR/CAS9 technology. Briefly, cells were transfected with Rab27a sgRNA CRISPR All-in-One-Lentivirus set (Applied Biological Materials (abm), Vancouver, Canada) at a MOI of 10. Cells were also transfected with Scrambled sgRNA CRISPR/Cas9 All-in-One Lentivirus to serve as a control. Properly transfected cells were selected for using puromycin antibiotic selection. Genomic cleavage was detected using the CRISPR Genomic Cleavage Detection Kit and standard protocol (abm, cat. No. G932). The following sgRNA sequence was used: sg1Rab27 CCA CCT GCA GTT ATG GGA CA

**HMGB-1 knockdown cell line—**For subculture, cells were maintained in DMEM medium supplemented with 10% FBS without antibiotics, in T-75 flasks. To obtain a high transfection efficiency, the reaction was carried out in complete medium for LLC cells, whereas 4T1 cells were switched to OptiMEM medium. For RNA interference (RNAi) experiments, LLC or 4T1 cells were subcultured in poly-L-lysine coated 6-well plates at a cell density of 8,000 cells/$cm^2$ and allowed to grow overnight. Next, 100 pmol/well of MISSION Endoribonuclease-Prepared siRNA (esiRNA) targeting either murine Hmgb1 or negative control (enhanced Green Fluorescent Protein (eGFP)) were delivered to each well using Lipofectamine 2000 reagent following manufacturer's directions. Briefly, 100 pmol of esiRNA and 10 μL Lipofectamine were separately diluted in 250 μL of Opti-MEM I

Reduced Serum Media each, incubated for 5 minutes at room temperature, gently mixed by pipetting up and down, and incubated for an additional 20 minutes at room temperature. Next, 500 μL of esiRNA/Lipofectamine complexes were added to each well, and cells were placed in a humidified incubator at 37 °C and 5% $CO_2$. After 24 hours post-transfection the growth medium was removed and replaced with Exosome-free growth medium (DMEM supplemented with 10% Exosome-free FBS). Cells were then allowed to grow for an additional 36 to 45 hours and the medium was harvested for exosome isolation as previously described. Random wells were used for total protein extraction and Western Blot assays for murine HMGB1 protein detection as described in the Western Blot methods section.

Hmgb1 esiRNA cDNA target sequence:

TCAACTAAACATGGGCAAAGGAGATCCTAAAAAGCCGAGAGGCAAAATGT
CCTCATATGCATTCTTTGTGCAAACTTGCCGGGAGGAGCACAAGAAGAAGC
ACCCGGATGCTTCTGTCAACTTCTCAGAGTTCTCCAAGAAGTGCTCAGAGA
GGTGGAAGACCATGTCTGCTAAAGAAAAGGGGAAATTTGAAGATATGGCA
AAGGCTGACAAGGCTCGTTATGAAAGAGAAATGAAAACCTACATCCCCCCC
AAAGGGGAGACCAAAAAGAAGTTCAAG GACCCCA

**Exosome purification, characterization, and quantification—**Supernatants were obtained from cancerous cell lines (LLC, 4T-1, MC38, B16-F10, A549, MCF-7, and S2-013) and non-cancerous epithelial cell lines (MLE-12 and HBEC) grown to 80% confluence over a 48-hour period in the appropriate growth media. For *in vivo* exosome isolation, primary tumors were excised, mechanically separated and enzymatically digested (collagenase (5g/L), Hyaluronidase(0.4g/L), DNAse I (0.15g/L)) for 35 minutes with rotation at 37°C. Cells were then cultured in complete DMEM as specified for cell lines. Exosomes were prepared as previously described (Gupta et al., 2018; Thery *et al.*, 2006). Briefly, the cell supernatants were spun once each at 2,000 × g and 10,000 × g. The supernatant was decanted and then carefully layered on top of 8mL of 30% sucrose prior to beging spun at 100,000 × g for 90 minutes. The supernatant was removed and the sucrose fraction containing the exosomes was washed with PBS and spun again at 100,000 × g for 90 minutes. Exosomes were collected using 150ul of PBS. Exosomes were then run through qEV 35nm single use columns (Izon Biosciences, Boston, MA) for further purification. Samples were run on the ZetaView PMX-120 Nanoparticle Tracking Analyzer (Particle Metrix, Inc.) to confirm exosome isolation via size verification and particle quantification. An aliquot of the purified exosomes was fixed in 2% paraformaldehyde for transmission electron microscopy (EM) using a conventional procedure and observed using an FEI Tecnai F20 (EM facility at the University of Alabama, Alabama, USA). The total exosome protein concentrations were determined by using the BCA Protein Assay kit (Thermo Fisher Scientific, Santa Clara, CA). The levels of lipoproteins including HDL and LDL and albumin in exosomes were determined by ELISA (Biorbyt). Finally, an Exo-check Antibody Array (Systems Bioscience, Palo Alto CA) was used to confirm proper surface marker expression profile for exosomes. Exosomes tested with the ToxinSensor single test kit (GenScript) were found to have an endotoxin level <0.25EU/mL.

**Isolation of Peritoneal Macrophages—**Peritoneal macrophages were harvested by peritoneal lavage as previously described (Ray and Dittel, 2010). Briefly, cold 3% FBS was injected into the peritoneal cavity and extracted after gentle agitation. The peritoneal cell suspension was centrifuged at 1600 r.p.m. After centrifugation, cells were resuspended in complete RPMI-1640 supplemented with 10% FBS (Atlanta Biologicals), and 1% Penicillin-Streptomycin Solution (Corning). Unless otherwise noted, cells were plated at a density of $5.0\times10^5$ cells/well in a 24 well plate. Cells were incubated at 37°C for 2 hours to allow macrophages to adhere to the plate. Floating cells were removed by two subsequent washes with PBS. For cell sorting, peritoneal macrophages were stained with Fixable Viability Dye and F4/80/FITC antibody (Biolegend) at 4°C for 30 min in the dark. Samples were then washed and resuspended in MACS running buffer. The samples were sorted on a FACS Aria gated on singlets followed by live, $F4/80^+$. Cells were immediately plated for use in subsequent experiments.

***In Vitro* Peritoneal Macrophage Culture—**Peritoneal macrophages were treated with MLE-12 Exo or LLC exo (40μg/mL) for 16 hours. After incubation, supernatant was removed and cells were washed briefly with PBS. Cells were harvested by adding 500μL Cell Stripper (Corning) and incubated for 1 minute at 37°C. RPMI-1640 was added to quench the reaction and cells were gently removed by scraping. For NF-κB experiments, macrophages were pre-treated with 0.2 μg/mL BAY-11-7082 for 1 hour at 37°C. Cells were then washed with PBS and then treated with exosome stimulation as normal. For the HMGB-1 studies, cells were stimulated with 10μg/mL recombinant murine HMGB-1 (Biolegend) for 16 hours. Macrophages were stimulated with 25μM linoleic acid (Sigma) for 16 hours. Peritoneal macrophages were sorted from C57BL/6 WT, $TLR2^{-/-}$ and $TLR7^{-/-}$ mice. $1\times10^5$ macrophages were plated and were stimulated with 4T1 TDE (5 μg/ml), exosomal RNA (140ng/mL), LPS (10 ng/ml), CpG ODN (1 μg/ml), and CL075 (1 μg/ml) for 16 hours. Culture supernatants were collected and assayed for TNF-α and IL-6 by ELISA.

**Flow cytometry—**Flow cytometry was performed on a BD FACS Canto (BD Biosciences). See Key Resources Table for full antibody reference list. For intracellular phosphorylation studies, peritoneal macrophages were seeded in a 24 well plate ($0.5\times10^6$/well). Cells were then stimulated with sodium L-lactate 20mM for the indicated time. Cells were then harvested from the plate and pelleted by centrifugation. They were then stained for viability. Cells were washed, pelleted, and resuspended in 100μl of 4% formaldehyde per 1 million cells and fixed for 15 minutes at room temperature. Cells were then washed with PBS. Ice cold methanol (2mL) was then added to the cells while gently vortexing to a make a final concentration of 90% methanol. Cells were permeabilized on ice for 10 minutes. Cells were then washed in excess PBS twice to remove methanol. Primary phospho-NF-κB p65 (Ser536) (93H1) (1:1600) and F4/80-APC was then added and incubated at RT for 1 hour. Cells were then washed in PBS twice. 100μl (0.625:100) secondary donkey anti-rabbit IgG Alexa Fluor 555 (Biolegend) was added and incubated at RT for 30 minutes in the dark. Cells were washed with PBS and ran on the BD FACS Canto (BD Biosciences).

**Mouse T cell proliferation assay—**Splenocytes from Ova-transgenic-I (OT-I) and Ova-transgenic-II (OT-II) mice were labeled with 5(6)-carboxyfluorescein diacetate succinimidyl

ester (CFSE cell trace, Thermo Fisher) at a concentration of 1 μM/mL according to manufacturer's instructions. Briefly, CFSE labelled cells were co-cultured with macrophages pre-treated with 40ug/mL exosomes (48 hours) at a 15:1 ratio. Macrophages were washed prior to T-cell addition to remove residual exosomes and recounted. OVA antigen was added at a final concentration of 25 μg/mL (OT-I) or 200 μg/mL (OT-II) for 48 or 72 hours, respectively. Blocking α-PD-1 antibody (40μg/mL, 60μg/mL) for OT-I and OT-II was added to culture along with OVA. Following culture cells were surfaced stained with CD4/APC and CD8/APC for 20 min. Cells were then fixed (Fixation Buffer, Biolegend) and permeabilized (Intracellular Staining Perm Wash Buffer, Biolgend) prior to overnight intracellular staining with IFN-γ.

**Quantitative PCR—**Total RNA was extracted from both isolated exosomes and stimulated cells using TRizol (Invitrogen) and processed according to manufacturer's instructions. Cells were harvested after 6-hour stimulation. Exosomal RNA was isolated from 60μg of LLC exosomes and quantified using a NanoDrop RNA 6000. cDNA was generated using the iScript cDNA Synthesis Kit (Bio-Rad). mRNA expression analysis was carried out using iQ SYBR Green (Bio-Rad). RNA concentration was quantified using NanoDrop RNA 6000 nano-assays and analyzed using the CFX Connect PCR Machine (Bio-Rad). See Table S2 for the primer sequences.

**Cytokine and ELISA measurement—**Supernatant was isolated from culture conditions, centrifuged at 6000rpm for 5 minutes to remove cellular debris and transferred to a new Eppendorf tube for storage at −20°C till use. Cytokine array was performed using the Proteome Profile Mouse Cytokine Array Panel A (R&D Systems Inc, Minneapolis, MN) according to the manufacturer's instructions. ELISA MAX IL-6, IL-10, and TNF-α kits (Biolegend) were used according to manufacturer's instructions.

**Western blot—**$F4/80^+$ cells were sorted using FACS Aria and the stimulated according to experimental design. For the HIF-1α western blot, cells were cultured in a hypoxia incubator for 24 hours prior to cell isolation. For exosome blots, exosomes were isolated according to the above protocol, quantified using BCA Assay, and then lysed using standard cell lysis buffer. Macrophage proteins were separated using SDS PAGE 10% Tris-HCl gels and transferred onto PVDF membranes (Millipore, Cat# IPVH00010). The blots were blocked with 5% BSA at room temperature for 1 hour and incubated overnight at 4°C with listed primary antibodies, followed by incubation with HRP-conjugated secondary antibodies (GE Healthcare) at room temperature for 1 hour. The membrane blots were developed with Amersham ECL Prime Western Blotting Detection Reagent (GE Healthcare, Cat # RPN2232) and detected through Medical Film Processor (Konica Minolta Medical & Graphic, Inc. Model: SRX-101A). We used Precision Plus Protein™ Kaleidoscope™ Prestained Protein Standards as a standard protein marker (Bio-Rad, Cat# 1610375)

**Immunofluorescence staining—**To detect exosome uptake in $F4/80^+$ peritoneal macrophages, cells were cultured with $GFP^+$ LLC exosomes (40μg/mL) for a one- or two-hour incubation on glass cover slips pre-coated with poly-L lysine. Slides were incubated overnight with rat anti-mouse F4/80 (1:100). Lung samples from *in vivo* experiments were

frozen in OCT and stored at −80°C. Sections of approximately 8 μm were fixed with cold acetone for 15 minutes followed by 30 minutes of air drying. Slides were then blocked using 20% FBS in PBS for 1 h. Primary Ab staining occurred overnight at 4°C in humidified staining container with antibodies to PD-L1 (1:100), CD11b (1:100), and F4/80 (1:100). For NF-κB translocation studies, peritoneal macrophages were plated on a glass cover slip in a 24 well dish and stimulated with sodium L-lactate for the indicated time. Cells were then washed with PBS, permeabilized with 0.3% Triton 100×, and stained with primary antibody NF-κB p65 (D14E12) (1:100) overnight at 4°C, washed with PBC and stained with secondary donkey anti-rabbit IgG Alexa Fluor 555 (Biolegend) (1:100) for 1 hour at room temperature. Fluorescent images were obtained using a Nikon confocal microscope A1R with appropriate lasers.

**LCFA Profiling—**For profile long chain fatty acids (LCFAs) and oxylipins in exosomes, freeze–thaw cycles were carried out to release LCFAs and oxylipins from exosomes. LCFAs and oxylipins were extracted using 50% ethanol, then purified and concentrated via solid phase extraction (SPE) for LC-MS analysis. LC-MS analysis was performed on Waters ACQUITY UPLC Systems with 2D Technology coupled with Waters Xevo TQ-S micro triple quadrupole mass spectrometer. LCFAs and oxylipins are separated by reversed-phase chromatography, then analyzed using single ion reaction (SIR) and multiple reaction monitoring (MRM) in negative ionization mode.

1. **Extraction of LCFAs and oxylipins:** Freeze–thaw cycles were carried out to release LCFAS and oxylipins from exosomes. 100 μL of ethanol was added into 100 μL of suspension of exosomes. The mixture was frozen in liquid nitrogen for 1 min and immediately thawed in ice for 1 min. This step was repeated 10 times. The SPE was carried out on Waters Oasis HLB cartridge (1 mL, 30 mg, 30μm). The cartridge was conditioned with 1 mL of methanol followed by 1 mL of water. 200 μL of lysate was loaded. After loading, the cartridge was washed with 1 mL of 5% methanol (*v/v*). LCFAs were eluted with 1 mL of methanol/acetonitrile (10/90, v/v). Extract was evaporated to dryness under a stream of nitrogen, then redissolved in 50 μL of 50% ethanol for LC-MS analysis.

2. **LC-MS analysis:** LCFAs and oxylipins measurement was carried out on Waters ACQUITY UPLC Systems coupled with Waters Xevo TQ-S micro triple quadrupole mass spectrometer. ACQUITY UPLC BEH C8 column (100 × 2.1 mm i.d., 1.7 μm) was used for LC separation. The LC separation was performed using a linear gradient from 30% to 99% of acetonitrile with 0.1% (*v/v*) acetic acid in 17 minutes, at a flow rate of 0.4 mL/min. The column temperature and injection volume were set at 40 °C and 5 μL, respectively. The mass spectrometer with an electrospray ionization (ESI) ion source was operated in negative mode with a capillary voltage of 3.5 kV. The source temperature was set at 300°C. Nitrogen was used as nebulizing gas at a flow of 650 L/Hr and argon was used as collision gas. Saturated fatty acids, monounsaturated acids and eicosadienoic acid were analyzed in single ion reaction (SIR) mode and others were analyzed in multiple reaction monitoring (MRM) mode. The SIR and MRM parameters were listed in Supplemental Table 3.

## Metabolism Assays

**Seahorse XF Cell Mito Stress Test:** An XF96e Analyzer (Agilent Technologies, Santa Clara, CA) was used to measure bioenergetic function in isolated peritoneal macrophages. Prior to the run, sorted peritoneal macrophages were plated at a concentration of $0.6\times10^5$cells/well. Cells were stimulated with MLE-12 or LLC exosomes (40 μg/mL) overnight. For all bioenergetic measurements, the culture media was changed 1 h prior to the assay run to unbuffered Dulbecco's Modified Eagle Medium (DMEM, pH 7.4) supplemented with 11 mM D-Glucose (Sigma cat. G7528), 2 mM L-glutamine (Mediatech cat. 61-030-RM), and 100 μM L-carnitine (Sigma cat. C0283). The final concentrations of oligomycin (port A), FCCP (port B), and antimycin A/rotenone (port C) were 2 μg/ml, 2.5 μM and 10 μM/1 μM, respectively. Three basal OCR measurements were recorded prior to injection of oligomycin. After recording the oligomycin-sensitive OCR, FCCP-sensitive rates were recorded. Finally, antimycin A/rotenone was injected to inhibit electron flow through the electron transport system. As a secondary measurement, extracellular acidification rate (ECAR) was also recorded, and 2-deoxyglucose was injected at final concentration of 250 μM (port D) to interrogate the contribution of glycolysis to ECAR.

**Seahorse glycolytic stress assay:** An XF96e Analyzer (Agilent Technologies, Santa Clara, CA) was used to measure glycolytic flux in isolated peritoneal macrophages ($0.6\times10^5$ cells/well). Cells were stimulated with MLE-12 or LLC exosomes (40 μg/mL) overnight with or without the presence of SEITU (2mM). The culture media was changed 1 h prior to the assay run to unbuffered Dulbecco's Modified Eagle Medium (DMEM, pH 7.4) supplemented with 2 mM L-glutamine (Agilent cat# 103575-100). A Seahorse XF Glycolysis Stress Test Kit was used and the final concentrations of Glucose (port A), Oligomycin (port B), and 2-deoxyglucose (port C) were 10mM, 2 μM and 50mM, respectively. Three basal ECAR measurements were recorded followed by an injection of a saturating level of glucose, measuring a glucose-induced response. This was followed by Oligomycin A, an ATP synthase inhibitor, which inhibits mitochondrial ATP production and shifts the energy production to glycolysis, revealing the cellular maximum glycolytic capacity. Finally, 2-deoxyglucose, a glucose analog, was injected to inhibit glucose binding to hexokinase, thus confirming extracellular rates to be a product of glycolysis. From these experimental measurements, measures of glycolysis, glycolytic reserve, glycolytic capacity, and non-glycolytic acidification were calculated.

**ROS staining:** For DCFDA staining, 100μL of 40μM DCFDA (abcam) was added to 100μL of cells ($1\times10^6$) and incubated in the dark at 37°C for 30 minutes. Cells were then washed with PBS and stained for flow cytometry.

***In vitro* metabolism assays:** Peritoneal macrophages were stimulated with MLE-12 or LLC Exo. (40μg/mL) for 16 hours. Cells were then washed and incubated in glucose free RPMI for 30 minutes before 2-NBDG (400μM, BioVision) was added. Cells were incubated with 2-NBDG for 15 minutes before washing and staining with viability dye and F4/80 for analysis via flow cytometry. The following concentrations of metabolic inhibitors or substrates were used for 16-hour cell culture: 2-deoxy-D-glucose (1mM, Sigma), SEITU (2–4mM, Cayman Chemical), Dimethyl-2-oxoglutarate (1mM-5mM, Sigma), Sodium-L-

Lactate (20mM, Sigma), AZD3965 (250nM, MedChemExpress). Levels of L-lactate in the supernatants were measured by L-Lactate Assay Kit I (Eton Bioscience, San Diego, CA) according to manufacturer's instructions.

***In vivo* Syngeneic Tumor Metastasis Model:** LLC ($0.5\times10^6$, in 100μl PBS) or Rab27$^{-/-}$/SCRAM 4T-1 ($1.2\times10^6$, in 100μl PBS) cells were injected subcutaneously into the flanks of C57BL/6 mice or orthotopically in the mammary glands of BALB/c mice, respectively. The mice were euthanized when the tumor diameter reached 10mm. Lung tissue was isolated and weighed prior to enzymatic digestion (collagenase (5g/L), Hyaluronidase (0.4g/L), DNAse I (0.15g/L)) for 35 minutes with rotation at 37°C. Following digestion, RBC's were lysed using ACK and resuspended in RPMI-1640 as a single cell suspension. Lung tissue was also fixed in OCT for hematoxylin and eosin staining or for confocal microscopic analysis.

**Exosome-mediated Metastasis Model:** The experiment was designed as previously described (Peinado et al., 2012). Briefly, 8–10 week old sex matched C57BL/6, TLR2$^{-/-}$, NOS2$^{-/-}$, HIF-1α$^{fl/fl}$;LysM-cre mice were subcutaneously injected in the flank with GFP$^+$ LLC ($0.5\times10^6$, 100μl PBS) cells. Five days post-injection, LLC exosomes, Pan02 exosomes, or control MLE-12 exosomes (10μg in 100μl PBS) were injected intravenously every three days for three weeks. Lung tissue samples were frozen in OCT at −80°C. Lung and liver tissue was enzymatically digested (collagenase (5g/L), Hyaluronidase(0.4g/L), DNAse I (0.15g/L)) for 35 minutes with rotation at 37°C prior to ACK lysis. Spleen cells were mechanically digested prior to ACK lysis. Whole lung cells ($5\times10^6$) were frozen in TRIzol for RNA extraction.

***In vivo* tracking of fluorescently labeled exosomes:** Purified exosomes were labeled according to the previous protocol (Wen et al., 2016). Briefly, exosomes were incubated for 10 minutes with Vybrant DiI (ThermoFisher, 1:1000 dilution). Excess dye was removed by washing in 20mL of PBS at 100,000 × g (90 minutes) to generate final DiI labeled exosomes. Exosomes were then intravenously injected into C57BL/6 mice (40 μg in 100μl PBS) and lung, bone marrow, and spleen were isolated 24 hours later and assessed for uptake via Flow cytometry.

***In vivo* $^{18}$FDG uptake experiment:** 8–10 week old C57BL/6 mice were injected i.v. with LLC exosomes (10μg, in 100μl PBS) every 3 days for 2 weeks. Mice were fasted for 12 hours prior to intraperitoneal injection with $^{18}$FDG. One hour after injection, the mice were euthanized, lungs were harvested and measured on a Biodex Atomlab™ 500 for radioactivity. Lung tissue was enzymatically digested (collagenase (5g/L), Hyaluronidase (0.4g/L), DNAse I (0.15g/L)) for 20 minutes with rotation at 37°C. Following digestion, RBC's were lysed using ACK. Cells were stained with primary Biotin anti-mouse CD19 (Biolegend,115504), secondary Streptavidin MicroBeads (Miltenyl Biotec,130-048-101), CD8a (Ly-2) MicroBeads (Miltenyl Biotec,130-049-401), CD4 (L3T4) (Miltenyl Biotec,130-049-201) for 15 minutes. Cells were then magnetically separated on an autoMACS Pro separator (Miltenyl Biotec) using the positive selection protocol. The negative fraction was then collected and read on a Biodex Atomlab™ 500 for radioactivity. Cells were then resuspended in Trizol and saved in the −80°C for RT-PCR.

**CyTOF Mass Cytometry Sample Preparation:** Mass cytometry antibodies (Key Resource Table) were either purchased pre-conjugated (Fluidigm) or were conjugated in house using MaxPar X8 Polymer Kits or MCP9 Polymer Kits (Fluidigm) according to the manufacturer's instruction. Single cell suspensions of lung and lymph node samples were isolated as described above. The samples were stained for viability with 5uM cisplatin (Fluidigm) in serum free RPMI1640 for 5 min at RT. The cells were washed with complete RPMI1640 for 5 min and stained with the complete antibody panel for 30 min at RT. Cells were then washed and fixed in 1.6% formaldehyde for 10 min at RT, and then incubated overnight in 125nM of Intercalator-Ir (Fluidigm) at 4°C.

**CyTOF Data Acquisition:** Prior to acquisition, samples were washed twice with Cell Staining Buffer (Fluidigm) and kept on ice until acquisition. Cells were then resuspended at a concentration of 1 million cells/mL in Cell Acquisition Solution containing a 1/9 dilution of EQ 4 Element Beads (Fluidigm). The samples were acquired on a Helios (Fluidigm) at an event rate of <500 events/second. After acquisition, the data were normalized using bead-based normalization in the CyTOF software. The data were gated to exclude residual normalization beads, debris, dead cells and doublets, leaving $DNA^{+}CD45^{+}Cisplatin^{low}$ events for subsequent clustering and high dimensional analyses. t-SNE plots were generated using FlowJo v.10.

***In vitro* human suppression assay:** The human T cell suppression assay was performed according to the previously published protocol (Singhal *et al.*, 2019). Briefly, donor PBMCs were sorted on a BD FACsAria for $CD14^{+}$ or $CD3^{+}$ expression. The $CD14^{+}$ cells were plated in a 96-well U-bottom plate ($0.5\times10^{5}$ cells/well) and stimulated with 40 μg/mL of HBEC or A549 exosomes for 48 hours. The 96 U-bottom plate had previously been coated with anti-human CD3 Abs (clone:OKT3) (1 μg/mL) in 100μL PBS at 37°C for 4 hours. The $CD3^{+}$ T cells were then labeled with 1 μM of the fluorescent dye 5,6-carboxyfluorescein diacetate succinimidyl ester (CFSE, Invitrogen), according to the manufacturer's instructions. Wells were gently washed twice with PBS before the addition of cells. CFSE-labeled responders ($1.0\times10^{5}$ cells/well) were mixed with previously stimulated $CD14^{+}$ cells in a 1:2 ratio and co-cultured for 4 days in the complete cell culture media. The CFSE signal was analyzed by flow cytometry on gated on both CD4+ and CD8+ lymphocytes.

To measure the IFN-γ production, $1.0\times10^{5}$ autologous sorted $CD3^{+}$ T cells stimulated with plate-bound anti-human CD3 Ab were co-incubated with previously stimulated $CD14^{+}$ subsets in a 1:2 ratio for 48 hours in 96 well U-bottom plate. BD GolgiStop and BD GolgiPlug were added into the cell cultures during the last 12 hours. Surface stained cells were fixed with Fixation Buffer (Biolegend) for 20 minutes. The fixed cells were permeabilized with Intracellular Staining Perm Wash Buffer (Biolegend) and then stained with the anti-human IFN-γ (Biolegend). The percent of intracellular IFN-γ positive $CD4^{+}$ and $CD8^{+}$ T cells was analyzed by flow cytometry.

***In vitro* human $CD14^{+}$ culture:** A549 exosomes or HBEC exosomes were added (40μg/mL) to previously sorted $CD14^{+}$ myeloid cells ($0.5\times10^{5}$, 48 well plate) and stimulated for 16 hours. TLR2 blocking antibody (TLR2 Monoclonal Antibody (TL2.1), eBioscience)

was added at 40μg/mL to sorted $CD14^+$ cells for 30 min at RT before stimulation with 40μg/mL of A549 exosomes. Sorted $CD14^+$ cells were pre-incubated with BAY-11-7082 (0.2μg/mL) for 1 hour prior to 16 hour stimulation with A549 exosomes. Sorted $CD14^+$ cells were stimulated with recombinant human HMGB-1 (4μg/mL and 10μg/mL, R&D Systems, Minneapolis, MN) for 16 hours. Metabolic assays were conducted using the same concentrations and procedures as the mouse protocols.

**Human YKT6 transfection:** For subculture, A549 cells were maintained in DMEM medium supplemented with 10% FBS without antibiotics, in T-75 flasks. To obtain sufficient medium for exosome isolation, 30 to 36 wells were seeded at a cell density of 30,000 cells/$cm^2$, and exosomes were isolated from approximately 12 million cells for each overexpression plasmid, yielding 100–120 mL of medium. For transfection experiments, A549 cells were subcultured in poly-L-lysine coated 6-well plates and allowed to grow overnight. Next, 2.5 μg of endotoxin-free C1-enhanced Green Fluorescent Protein (C1-eGFP) or C1-eGFP N-terminal fused to the human YKT6 gene coding sequence (C1-eGFP-huYKT6) overexpression plasmids were delivered to each well using Lipofectamine 3000 reagent following manufacturer's directions. The plasmids were kindly provided by Dr. Gabriela C. Piso (McGrath et al., 2021). Briefly, 2.5 μg of DNA and 7.5 μL Lipofectamine were separately diluted in 125 μL of Opti-MEM I Reduced Serum Media each, incubated for 5 minutes at room temperature, gently mixed altogether, and incubated for an additional 20 minutes at room temperature. Next, 250 μL of DNA/Lipofectamine complexes were added to each well, and cells were placed in a humidified incubator at 37 °C and 5% $CO_2$. After 16 hours post-transfection the growth medium was removed and replaced with exosome-depleted growth medium (DMEM supplemented with 10% exosome-depleted FBS). Cells were then allowed to grow for an additional 72–96 hours, and the medium was harvested for exosome isolation. Random wells were used for total protein extraction followed by Western Blot experiments using anti-human YKT6 or anti-β-actin antibody.

## QUANTIFICATION AND STATISTICAL ANALYSIS

**Statistics—**All results were repeated at least three independent experiments or as indicated. All statistical analyses were performed using GraphPad PRISM software unless otherwise noted (version 8.0, Irvine, CA, USA). No statistical methods were used to predetermine the sample size. No other data points or samples were excluded from the study. For in vitro assays, triplicates were used for statistical analysis, *n* correspond to the independent repeat. All experiments that compared two conditions used unpaired Student's *t* tests or as indicated while those that compared three or more conditions used a one-way ANOVA with multiple comparisons. A value of $p < 0.05$ (two-sided) was considered statistically significant. Data are represented as mean ± SEM. The statistical parameters can be found in the figures and figure legends.

**PCA analysis—**To collectively assess the relationships of myeloid and T cell markers of human samples screened in this study in the context of disease status, we conducted Principal Component Analysis (PCA) using estimated cell marker percentages in each of the 9 NSCLC and 10 HD samples. Within the R statistical environment (https://www.r-project.org/), PCA was performed using the prcomp() function, with the "scale" parameter

set to “TRUE”. The PCA plot was generated using the R package “factoextra”, including 95% confidence ellipses. To assess the statistical association of the first principal component and disease status, linear regression was conducted using the R lm() function, in which disease status of each NSCLC and HD subject was treated as the dependent variable and the first principle component scores were treated as the independent variable.

**TCGA Nodal Status Analysis—**RNA-seq data was downloaded from TCGA for several cancer types. The cases with nodal status were kept. Deseq 2 was run on the raw counts between cases with nodal status N0 and all other nodal status (N1,N2,N3). Plots were made with Deseq2’s function plotCounts with counts normalized by the library size. The p value reported was adjusted to correct for false positives due to multiple testing.

## Supplementary Material

Refer to Web version on PubMed Central for supplementary material.

## Acknowledgements:

The authors thank Dr. Douglas C. Dean for critical reading of this manuscript, J. Noe for his biochemical and metabolic expertise, S. Balasubramanian for assisting in data collection, and Dr. Aqil Farrukh to assist nanoparticle tracking analysis. This work was supported by the NIH R01CA213990, P01CA163223, and the Kentucky Lung Cancer Research Program (J.Y.). CY, ZW, and JH were supported by the National Natural Science Foundation of China (No. 81930079). CD, DT, CW, and JY were supported in part by the NIH P20GM135004.

## References:

Apicella M, Giannoni E, Fiore S, Ferrari KJ, Fernandez-Perez D, Isella C, Granchi C, Minutolo F, Sottile A, Comoglio PM, et al. (2018). Increased Lactate Secretion by Cancer Cells Sustains Non-cell-autonomous Adaptive Resistance to MET and EGFR Targeted Therapies. Cell metabolism 28, 848–865 e846. 10.1016/j.cmet.2018.08.006. [PubMed: 30174307]

Asgarova A, Asgarov K, Godet Y, Peixoto P, Nadaradjane A, Boyer-Guittaut M, Galaine J, Guenat D, Mougey V, Perrard J, et al. (2018). PD-L1 expression is regulated by both DNA methylation and NF-kB during EMT signaling in non-small cell lung carcinoma. Oncoimmunology 7, e1423170–e1423170. 10.1080/2162402X.2017.1423170. [PubMed: 29721376]

Aucott H, Sowinska A, Harris HE, and Lundback P (2018). Ligation of free HMGB1 to TLR2 in the absence of ligand is negatively regulated by the C-terminal tail domain. Mol Med 24, 19. 10.1186/s10020-018-0021-x. [PubMed: 30134807]

Bader JE, Enos RT, Velázquez KT, Carson MS, Nagarkatti M, Nagarkatti PS, Chatzistamou I, Davis JM, Carson JA, Robinson CM, and Murphy EA (2018). Macrophage depletion using clodronate liposomes decreases tumorigenesis and alters gut microbiota in the AOM/DSS mouse model of colon cancer. Am J Physiol Gastrointest Liver Physiol 314, G22–G31. 10.1152/ajpgi.00229.2017. [PubMed: 29025731]

Bardi GT, Smith MA, and Hood JL (2018). Melanoma exosomes promote mixed M1 and M2 macrophage polarization. Cytokine 105, 63–72. 10.1016/j.cyto.2018.02.002. [PubMed: 29459345]

Binnewies M, Roberts EW, Kersten K, Chan V, Fearon DF, Merad M, Coussens LM, Gabrilovich DI, Ostrand-Rosenberg S, Hedrick CC, et al. (2018). Understanding the tumor immune microenvironment (TIME) for effective therapy. Nat Med 24, 541–550. 10.1038/s41591-018-0014-x. [PubMed: 29686425]

Borghaei H, Paz-Ares L, Horn L, Spigel DR, Steins M, Ready NE, Chow LQ, Vokes EE, Felip E, Holgado E, et al. (2015). Nivolumab versus Docetaxel in Advanced Nonsquamous Non-Small-Cell Lung Cancer. The New England journal of medicine 373, 1627–1639. 10.1056/NEJMoa1507643. [PubMed: 26412456]

Boukouris S, and Mathivanan S (2015). Exosomes in bodily fluids are a highly stable resource of disease biomarkers. Proteomics Clin Appl 9, 358–367. 10.1002/prca.201400114. [PubMed: 25684126]

Bretz NP, Ridinger J, Rupp AK, Rimbach K, Keller S, Rupp C, Marme F, Umansky L, Umansky V, Eigenbrod T, et al. (2013). Body fluid exosomes promote secretion of inflammatory cytokines in monocytic cells via Toll-like receptor signaling. J Biol Chem 288, 36691–36702. 10.1074/jbc.M113.512806. [PubMed: 24225954]

Chen G, Huang AC, Zhang W, Zhang G, Wu M, Xu W, Yu Z, Yang J, Wang B, Sun H, et al. (2018). Exosomal PD-L1 contributes to immunosuppression and is associated with anti-PD-1 response. Nature 560, 382–386. 10.1038/s41586-018-0392-8. [PubMed: 30089911]

Chin AR, and Wang SE (2016). Cancer Tills the Premetastatic Field: Mechanistic Basis and Clinical Implications. Clinical cancer research : an official journal of the American Association for Cancer Research 22, 3725–3733. 10.1158/1078-0432.ccr-16-0028. [PubMed: 27252414]

Colegio OR, Chu NQ, Szabo AL, Chu T, Rhebergen AM, Jairam V, Cyrus N, Brokowski CE, Eisenbarth SC, Phillips GM, et al. (2014). Functional polarization of tumour-associated macrophages by tumour-derived lactic acid. Nature 513, 559–563. 10.1038/nature13490. [PubMed: 25043024]

Everts B, Amiel E, van der Windt GJW, Freitas TC, Chott R, Yarasheski KE, Pearce EL, and Pearce EJ (2012). Commitment to glycolysis sustains survival of NO-producing inflammatory dendritic cells. Blood 120, 1422–1431. 10.1182/blood-2012-03-419747. [PubMed: 22786879]

Feng W, Dean DC, Hornicek FJ, Shi H, and Duan Z (2019). Exosomes promote pre-metastatic niche formation in ovarian cancer. Molecular cancer 18, 124. 10.1186/s12943-019-1049-4. [PubMed: 31409361]

Fischer K, Hoffmann P, Voelkl S, Meidenbauer N, Ammer J, Edinger M, Gottfried E, Schwarz S, Rothe G, Hoves S, et al. (2007). Inhibitory effect of tumor cell-derived lactic acid on human T cells. Blood 109, 3812–3819. 10.1182/blood-2006-07-035972. [PubMed: 17255361]

Fleming V, Hu X, Weller C, Weber R, Groth C, Riester Z, Huser L, Sun Q, Nagibin V, Kirschning C, et al. (2019). Melanoma Extracellular Vesicles Generate Immunosuppressive Myeloid Cells by Upregulating PD-L1 via TLR4 Signaling. Cancer Res 79, 4715–4728. 10.1158/0008-5472.CAN-19-0053. [PubMed: 31337655]

Gabrusiewicz K, Li X, Wei J, Hashimoto Y, Marisetty AL, Ott M, Wang F, Hawke D, Yu J, Healy LM, et al. (2018). Glioblastoma stem cell-derived exosomes induce M2 macrophages and PD-L1 expression on human monocytes. Oncoimmunology 7, e1412909. 10.1080/2162402x.2017.1412909. [PubMed: 29632728]

Gupta S, Rawat S, Arora V, Kottarath SK, Dinda AK, Vaishnav PK, Nayak B, and Mohanty S (2018). An improvised one-step sucrose cushion ultracentrifugation method for exosome isolation from culture supernatants of mesenchymal stem cells. Stem Cell Res Ther 9, 180–180. 10.1186/s13287-018-0923-0. [PubMed: 29973270]

Haderk F, Schulz R, Iskar M, Cid LL, Worst T, Willmund KV, Schulz A, Warnken U, Seiler J, Benner A, et al. (2017). Tumor-derived exosomes modulate PD-L1 expression in monocytes. Sci Immunol 2. 10.1126/sciimmunol.aah5509.

Headley MB, Bins A, Nip A, Roberts EW, Looney MR, Gerard A, and Krummel MF (2016). Visualization of immediate immune responses to pioneer metastatic cells in the lung. Nature 531, 513–517. 10.1038/nature16985. [PubMed: 26982733]

Herbst RS, Morgensztern D, and Boshoff C (2018). The biology and management of non-small cell lung cancer. Nature 553, 446. 10.1038/nature2518310.1038/nature25183https://www.nature.com/articles/nature25183#supplementary-informationhttps://www.nature.com/articles/nature25183#supplementary-information . [PubMed: 29364287]

Hessvik NP, and Llorente A (2018). Current knowledge on exosome biogenesis and release. Cell Mol Life Sci 75, 193–208. 10.1007/s00018-017-2595-9. [PubMed: 28733901]

Hoshino A, Costa-Silva B, Shen TL, Rodrigues G, Hashimoto A, Tesic Mark M, Molina H, Kohsaka S, Di Giannatale A, Ceder S, et al. (2015). Tumour exosome integrins determine organotropic metastasis. Nature 527, 329–335. 10.1038/nature15756. [PubMed: 26524530]

Huang S, Rutkowsky JM, Snodgrass RG, Ono-Moore KD, Schneider DA, Newman JW, Adams SH, and Hwang DH (2012). Saturated fatty acids activate TLR-mediated proinflammatory signaling pathways. J Lipid Res 53, 2002–2013. 10.1194/jlr.D029546. [PubMed: 22766885]

Hwang DH, Kim JA, and Lee JY (2016). Mechanisms for the activation of Toll-like receptor 2/4 by saturated fatty acids and inhibition by docosahexaenoic acid. Eur J Pharmacol 785, 24–35. 10.1016/j.ejphar.2016.04.024. [PubMed: 27085899]

Jablonski KA, Amici SA, Webb LM, Ruiz-Rosado Jde D, Popovich PG, Partida-Sanchez S, and Guerau-de-Arellano M (2015). Novel Markers to Delineate Murine M1 and M2 Macrophages. PloS one 10, e0145342. 10.1371/journal.pone.0145342. [PubMed: 26699615]

Jeong H, Kim S, Hong BJ, Lee CJ, Kim YE, Bok S, Oh JM, Gwak SH, Yoo MY, Lee MS, et al. (2019). Tumor-Associated Macrophages Enhance Tumor Hypoxia and Aerobic Glycolysis. Cancer research 79, 795–806. 10.1158/0008-5472.can-18-2545. [PubMed: 30610087]

Kalluri R (2016). The biology and function of exosomes in cancer. J Clin Invest 126, 1208–1215. 10.1172/jci81135. [PubMed: 27035812]

Lastwika KJ, Wilson W 3rd, Li QK, Norris J, Xu H, Ghazarian SR, Kitagawa H, Kawabata S, Taube JM, Yao S, et al. (2016). Control of PD-L1 Expression by Oncogenic Activation of the AKT-mTOR Pathway in Non-Small Cell Lung Cancer. Cancer research 76, 227–238. 10.1158/0008-5472.can-14-3362. [PubMed: 26637667]

Li I, and Nabet BY (2019). Exosomes in the tumor microenvironment as mediators of cancer therapy resistance. Molecular cancer 18, 32. 10.1186/s12943-019-0975-5. [PubMed: 30823926]

Lin H, Wei S, Hurt EM, Green MD, Zhao L, Vatan L, Szeliga W, Herbst R, Harms PW, Fecher LA, et al. (2018). Host expression of PD-L1 determines efficacy of PD-L1 pathway blockade-mediated tumor regression. J Clin Invest 128, 805–815. 10.1172/jci96113. [PubMed: 29337305]

Linde N, Casanova-Acebes M, Sosa MS, Mortha A, Rahman A, Farias E, Harper K, Tardio E, Reyes Torres I, Jones J, et al. (2018). Macrophages orchestrate breast cancer early dissemination and metastasis. Nature communications 9, 21. 10.1038/s41467-017-02481-5.

Liu Y, and Cao X (2016). Characteristics and Significance of the Pre-metastatic Niche. Cancer cell 30, 668–681. 10.1016/j.ccell.2016.09.011. [PubMed: 27846389]

Liu Y, Gu Y, Han Y, Zhang Q, Jiang Z, Zhang X, Huang B, Xu X, Zheng J, and Cao X (2016). Tumor Exosomal RNAs Promote Lung Pre-metastatic Niche Formation by Activating Alveolar Epithelial TLR3 to Recruit Neutrophils. Cancer cell 30, 243–256. 10.1016/j.ccell.2016.06.021. [PubMed: 27505671]

Ludwig S, Floros T, Theodoraki M-N, Hong C-S, Jackson EK, Lang S, and Whiteside TL (2017). Suppression of Lymphocyte Functions by Plasma Exosomes Correlates with Disease Activity in Patients with Head and Neck Cancer. Clinical cancer research : an official journal of the American Association for Cancer Research 23, 4843–4854. 10.1158/1078-0432.CCR-16-2819. [PubMed: 28400428]

Lux A, Kahlert C, Grutzmann R, and Pilarsky C (2019). c-Met and PD-L1 on Circulating Exosomes as Diagnostic and Prognostic Markers for Pancreatic Cancer. International journal of molecular sciences 20. 10.3390/ijms20133305.

Mascaux C, Angelova M, Vasaturo A, Beane J, Hijazi K, Anthoine G, Buttard B, Rothe F, Willard-Gallo K, Haller A, et al. (2019). Immune evasion before tumour invasion in early lung squamous carcinogenesis. Nature 571, 570–575. 10.1038/s41586-019-1330-0. [PubMed: 31243362]

McGrath K, Agarwal S, Tonelli M, Dergai M, Gaeta AL, Shum AK, Lacoste J, Zhang Y, Wen W, Chung D, et al. (2021). A conformational switch driven by phosphorylation regulates the activity of the evolutionarily conserved SNARE Ykt6. Proc Natl Acad Sci U S A 118. 10.1073/pnas.2016730118.

Muhsin-Sharafaldine M-R, Saunderson SC, Dunn AC, Faed JM, Kleffmann T, and McLellan AD (2016). Procoagulant and immunogenic properties of melanoma exosomes, microvesicles and apoptotic vesicles. Oncotarget 7, 56279–56294. 10.18632/oncotarget.10783. [PubMed: 27462921]

Peinado H, Alečković M, Lavotshkin S, Matei I, Costa-Silva B, Moreno-Bueno G, Hergueta-Redondo M, Williams C, García-Santos G, Ghajar C, et al. (2012). Melanoma exosomes educate bone marrow progenitor cells toward a pro-metastatic phenotype through MET. Nature medicine 18, 883–891. 10.1038/nm.2753.

Penny HL, Sieow JL, Adriani G, Yeap WH, See Chi Ee P, San Luis B, Lee B, Lee T, Mak SY, Ho YS, et al. (2016). Warburg metabolism in tumor-conditioned macrophages promotes metastasis in human pancreatic ductal adenocarcinoma. Oncoimmunology 5, e1191731. 10.1080/2162402x.2016.1191731. [PubMed: 27622062]

Poggio M, Hu T, Pai CC, Chu B, Belair CD, Chang A, Montabana E, Lang UE, Fu Q, Fong L, and Blelloch R (2019). Suppression of Exosomal PD-L1 Induces Systemic Anti-tumor Immunity and Memory. Cell 177, 414–427 e413. 10.1016/j.cell.2019.02.016. [PubMed: 30951669]

Ray A, and Dittel BN (2010). Isolation of mouse peritoneal cavity cells. J Vis Exp. 10.3791/1488.

Ricklefs FL, Alayo Q, Krenzlin H, Mahmoud AB, Speranza MC, Nakashima H, Hayes JL, Lee K, Balaj L, Passaro C, et al. (2018). Immune evasion mediated by PD-L1 on glioblastoma-derived extracellular vesicles. Science advances 4, eaar2766. 10.1126/sciadv.aar2766. [PubMed: 29532035]

Ruiz-Martinez M, Navarro A, Marrades RM, Vinolas N, Santasusagna S, Munoz C, Ramirez J, Molins L, and Monzo M (2016). YKT6 expression, exosome release, and survival in non-small cell lung cancer. Oncotarget 7, 51515–51524. 10.18632/oncotarget.9862. [PubMed: 27285987]

Salimian Rizi B, Achreja A, and Nagrath D (2017). Nitric Oxide: The Forgotten Child of Tumor Metabolism. Trends in cancer 3, 659–672. 10.1016/j.trecan.2017.07.005. [PubMed: 28867169]

Seo JB, Im JG, Goo JM, Chung MJ, and Kim MY (2001). Atypical pulmonary metastases: spectrum of radiologic findings. Radiographics : a review publication of the Radiological Society of North America, Inc 21, 403–417. 10.1148/radiographics.21.2.g01mr17403.

Sica A, and Mantovani A (2012). Macrophage plasticity and polarization: in vivo veritas. J Clin Invest 122, 787–795. 10.1172/jci59643. [PubMed: 22378047]

Silvestri GA, Gonzalez AV, Jantz MA, Margolis ML, Gould MK, Tanoue LT, Harris LJ, and Detterbeck FC (2013). Methods for staging non-small cell lung cancer: Diagnosis and management of lung cancer, 3rd ed: American College of Chest Physicians evidence-based clinical practice guidelines. Chest 143, e211S–e250S. 10.1378/chest.12-2355. [PubMed: 23649440]

Singhal S, Stadanlick J, Annunziata MJ, Rao AS, Bhojnagarwala PS, O'Brien S, Moon EK, Cantu E, Danet-Desnoyers G, Ra H-J, et al. (2019). Human tumor-associated monocytes/macrophages and their regulation of T cell responses in early-stage lung cancer. Science Translational Medicine 11, eaat1500. 10.1126/scitranslmed.aat1500. [PubMed: 30760579]

Takada K, Toyokawa G, Yoneshima Y, Tanaka K, Okamoto I, Shimokawa M, Wakasu S, Haro A, Osoegawa A, Tagawa T, et al. (2019). 18F-FDG uptake in PET/CT is a potential predictive biomarker of response to anti-PD-1 antibody therapy in non-small cell lung cancer. Scientific reports 9, 13362. 10.1038/s41598-019-50079-2. [PubMed: 31527660]

Tang H, Liang Y, Anders RA, Taube JM, Qiu X, Mulgaonkar A, Liu X, Harrington SM, Guo J, Xin Y, et al. (2018). PD-L1 on host cells is essential for PD-L1 blockade-mediated tumor regression. J Clin Invest 128, 580–588. 10.1172/jci96061. [PubMed: 29337303]

Theodoraki MN, Yerneni SS, Hoffmann TK, Gooding WE, and Whiteside TL (2018). Clinical Significance of PD-L1(+) Exosomes in Plasma of Head and Neck Cancer Patients. Clinical cancer research : an official journal of the American Association for Cancer Research 24, 896–905. 10.1158/1078-0432.ccr-17-2664. [PubMed: 29233903]

Thery C, Amigorena S, Raposo G, and Clayton A (2006). Isolation and characterization of exosomes from cell culture supernatants and biological fluids. Current protocols in cell biology Chapter 3, Unit 3 22. 10.1002/0471143030.cb0322s30. [PubMed: 18228490]

van Niel G, D'Angelo G, and Raposo G (2018). Shedding light on the cell biology of extracellular vesicles. Nature reviews. Molecular cell biology 19, 213–228. 10.1038/nrm.2017.125. [PubMed: 29339798]

Vegran F, Boidot R, Michiels C, Sonveaux P, and Feron O (2011). Lactate influx through the endothelial cell monocarboxylate transporter MCT1 supports an NF-kappaB/IL-8 pathway that drives tumor angiogenesis. Cancer Res 71, 2550–2560. 10.1158/0008-5472.CAN-10-2828. [PubMed: 21300765]

Wang W, Chapman NM, Zhang B, Li M, Fan M, Laribee RN, Zaidi MR, Pfeffer LM, Chi H, and Wu Z-H (2019). Upregulation of PD-L1 via HMGB1-activated IRF3 and NF-kB

contributes to UV radiation-induced immune suppression. Cancer research, canres.3134.2018. 10.1158/0008-5472.CAN-18-3134.

Wen SW, Sceneay J, Lima LG, Wong CS, Becker M, Krumeich S, Lobb RJ, Castillo V, Wong KN, Ellis S, et al. (2016). The Biodistribution and Immune Suppressive Effects of Breast Cancer-Derived Exosomes. Cancer research 76, 6816–6827. 10.1158/0008-5472.can-16-0868. [PubMed: 27760789]

Wu L, and Yang L (2018). The function and mechanism of HMGB1 in lung cancer and its potential therapeutic implications. Oncol Lett 15, 6799–6805. 10.3892/ol.2018.8215. [PubMed: 29725415]

Xiang X, Liu Y, Zhuang X, Zhang S, Michalek S, Taylor DD, Grizzle W, and Zhang H-G (2010). TLR2-mediated expansion of MDSCs is dependent on the source of tumor exosomes. Am J Pathol 177, 1606–1610. 10.2353/ajpath.2010.100245. [PubMed: 20802178]

Yang H, Zhang H, Ge S, Ning T, Bai M, Li J, Li S, Sun W, Deng T, Zhang L, et al. (2018). Exosome-Derived miR-130a Activates Angiogenesis in Gastric Cancer by Targeting C-MYB in Vascular Endothelial Cells. Molecular therapy : the journal of the American Society of Gene Therapy 26, 2466–2475. 10.1016/j.ymthe.2018.07.023. [PubMed: 30120059]

Yu M, Wang H, Ding A, Golenbock DT, Latz E, Czura CJ, Fenton MJ, Tracey KJ, and Yang H (2006). HMGB1 signals through toll-like receptor (TLR) 4 and TLR2. Shock 26, 174–179. 10.1097/01.shk.0000225404.51320.82. [PubMed: 16878026]

Zhang D, Tang Z, Huang H, Zhou G, Cui C, Weng Y, Liu W, Kim S, Lee S, Perez-Neut M, et al. (2019). Metabolic regulation of gene expression by histone lactylation. Nature 574, 575–580. 10.1038/s41586-019-1678-1. [PubMed: 31645732]

Zhang X, Shi H, Yuan X, Jiang P, Qian H, and Xu W (2018). Tumor-derived exosomes induce N2 polarization of neutrophils to promote gastric cancer cell migration. Molecular cancer 17, 146. 10.1186/s12943-018-0898-6. [PubMed: 30292233]

Zhang X, Zeng Y, Qu Q, Zhu J, Liu Z, Ning W, Zeng H, Zhang N, Du W, Chen C, and Huang JA (2017). PD-L1 induced by IFN-gamma from tumor-associated macrophages via the JAK/STAT3 and PI3K/AKT signaling pathways promoted progression of lung cancer. International journal of clinical oncology 22, 1026–1033. 10.1007/s10147-017-1161-7. [PubMed: 28748356]

**Highlights:**

1. TDE stimulate *de novo* synthesis of PD-L1 in macrophages
2. TDE activate NF-κB that augments glycolysis leading to increased lactate production
3. Lactate drives PD-L1 expression through the NF-κB pathway
4. Macrophage PD-L1 in the dLNs correlates with YKT6 expression levels in primary NSCLC

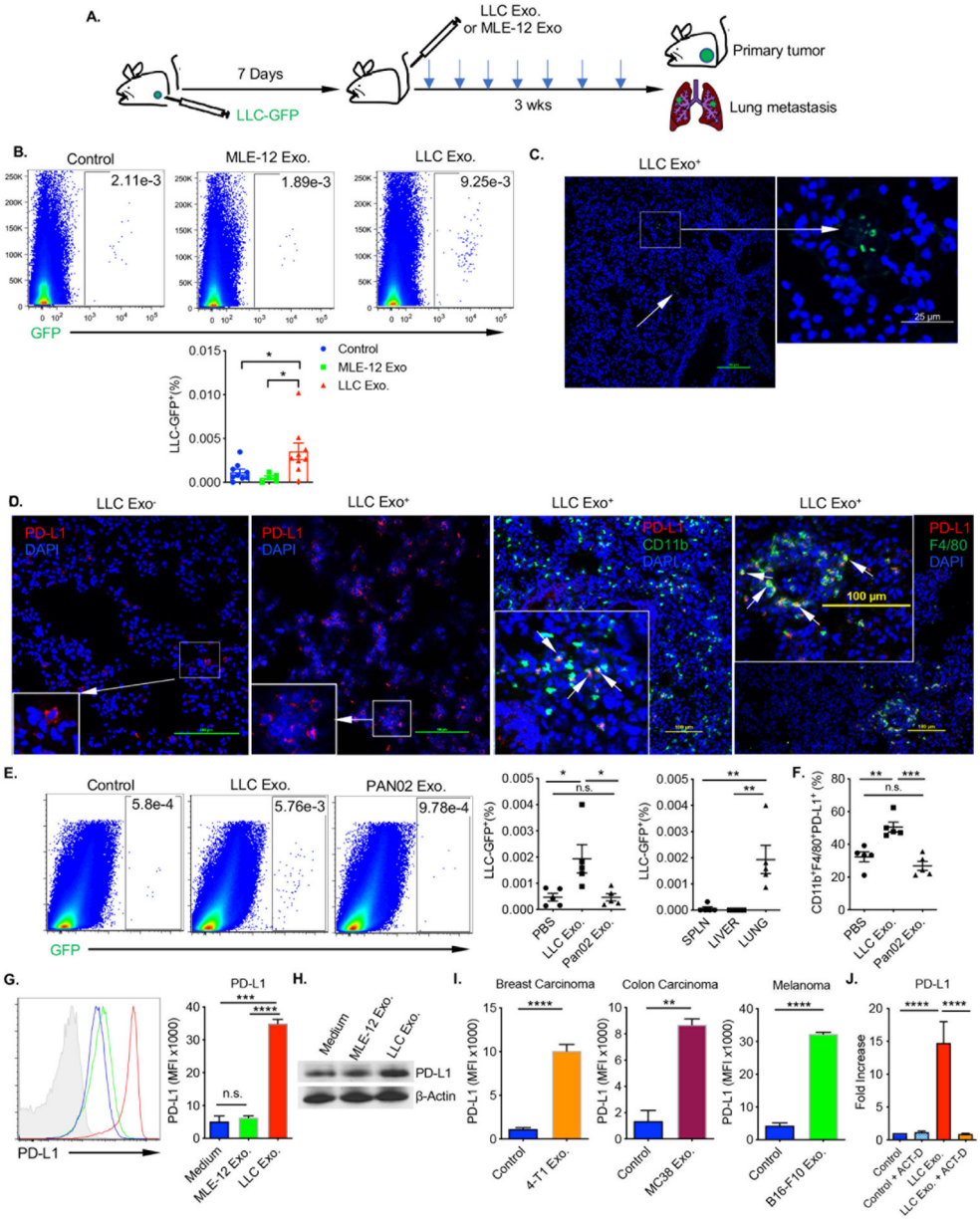


**Figure 1. The effect of TDE on macrophages in a pre-metastatic niche.**

**(A)** Schematic for experimental design (B-E). **(B)** Micro-metastatic burden quantified by LLC-GFP% in the lungs of s.c. GFP-LLC tumor-bearing mice treated i.v. with MLE-12 or LLC exosomes. Representative dot plots of GFP expression in the lungs and summarized data of LLC-GFP% are shown. Each dot represents data from one mouse. *p<0.05, (one-way ANOVA with multiple comparisons). **(C)** Confocal microscopic analysis of lung $GFP^+$ micro-metastases from primary s.c. LLC tumor-bearing mice. **(D)** Confocal microscopic analysis of PD-L1 expression in LLC $Exo^-$ or LLC $Exo^+$ treated lungs (left) and PD-L1 co-expression with CD11b and F4/80 in LLC $Exo^+$ mice (right). Scale bar=100μm. **(E)** Micro-metastatic burden quantified by LLC-GFP% in the lungs of s.c. GFP-LLC tumor-bearing mice treated i.v. with LLC or Pan02 Exo.. Representative dot plots of GFP expression in the

lungs (left) and summarized data of LLC-GFP% in the lungs (middle) and tissue specific LLC-GFP% of LLC Exo. treated mice (right) are shown. *p<0.05, **p<0.01, ***p<0.001 (one-way ANOVA with multiple comparisons). **(F)** Percentage of $CD11b^{+}F4/80^{+}PD\text{-}L1^{+}$ IM in the lungs of control and exosome treated mice. **(G)** Expression of PD-L1 by flow cytometry in peritoneal macrophages stimulated with MLE-12 Exo. or LLC Exo.. Representative histograms and summarized MFI are shown (n=3). MFI= mean fluorescent intensity. ***p<0.001, ****p<0.001, one-way ANOVA with multiple comparisons. **(H)** Representative western blot showing increased PD-L1 expression in macrophages treated with LLC Exo. for 16 hours. **(I)** PD-L1 expression by flow cytometry on macrophages treated with exosomes from 4-T1, MC38, and B16-F10 cell lines. n=3. **(J)** The mRNA expression of PD-L1 in macrophages stimulated with LLC Exo. with pre-treatment of actinomycin D (ACT-D). n=3. Data was normalized to control expression level. The data are shown as mean ± SEM. **p<0.01, ***p<0.001, ****p<0.001 (unpaired student's t test). See also Figure S1.

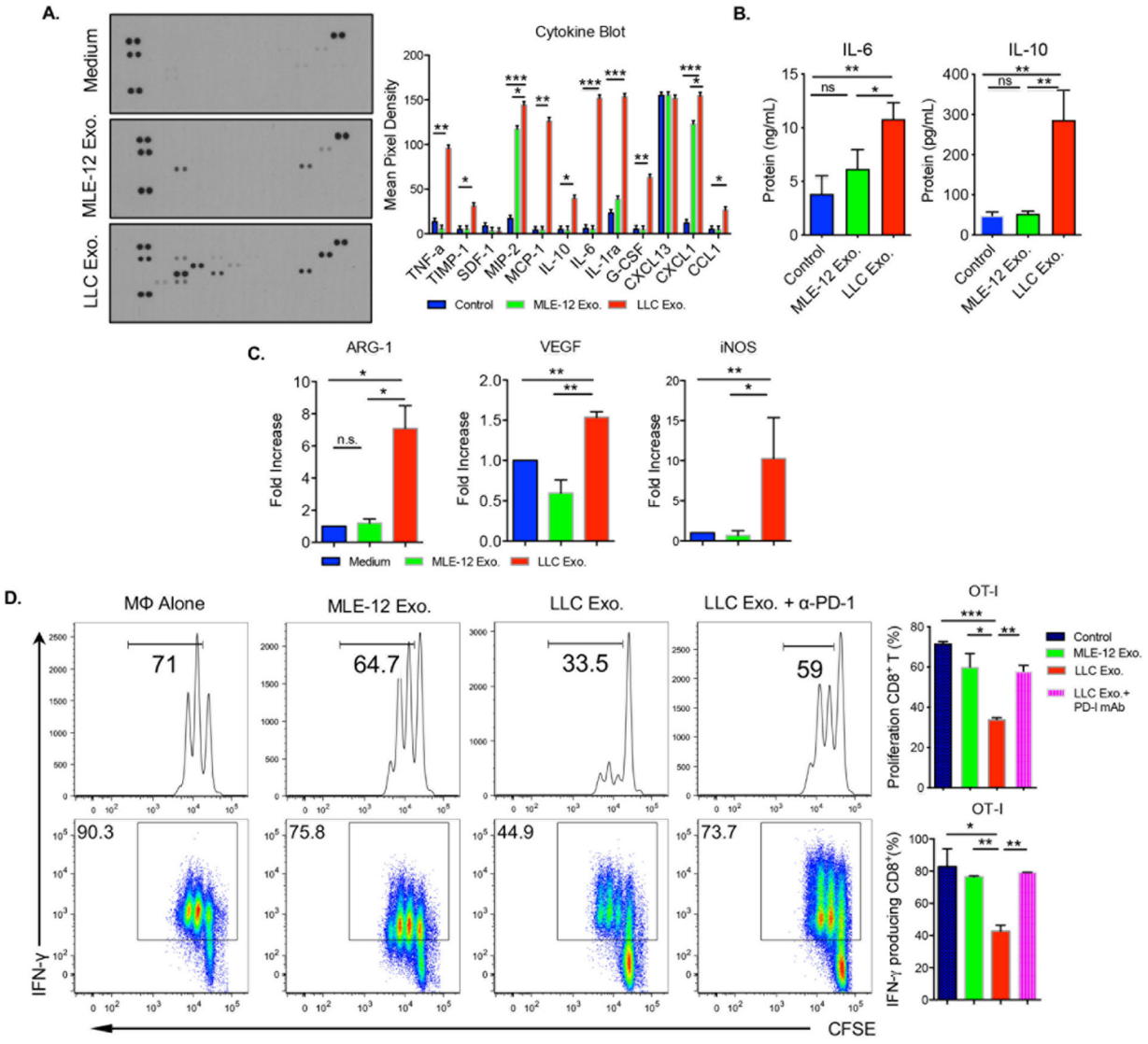


**Figure 2. TDE polarize macrophages towards an immunosuppressive phenotype.**

**(A)** Representative cytokine array panels of supernatants taken from 16-hour culture of peritoneal macrophages stimulated with media alone (top), MLE-12 exosomes (middle), or LLC exosomes (bottom). Representative plots and summarized mean pixel density of each protein are shown (n=3). **(B)** IL-6 and IL-10 concentration detected by ELISA from supernatants of macrophages stimulated with MLE-12 and LLC exosomes (n=3). **(C)** The mRNA expression levels of *Arg-1*, *VEGF*, and *iNOS* in peritoneal macrophages treated alone or with MLE-12 or LLC exosomes (n=3). **(D)** LLC exosome polarized macrophages suppress OT-I T-cell proliferation (top) and IFN-γ production (bottom) in a PD-L1 dependent manner. Representative histograms and summarized data are shown (n=3). The data are shown as mean ± SEM. *p<0.05, **p<0.01, ***p<0.001 (one-way ANOVA with multiple comparisons). See also Figure S2.

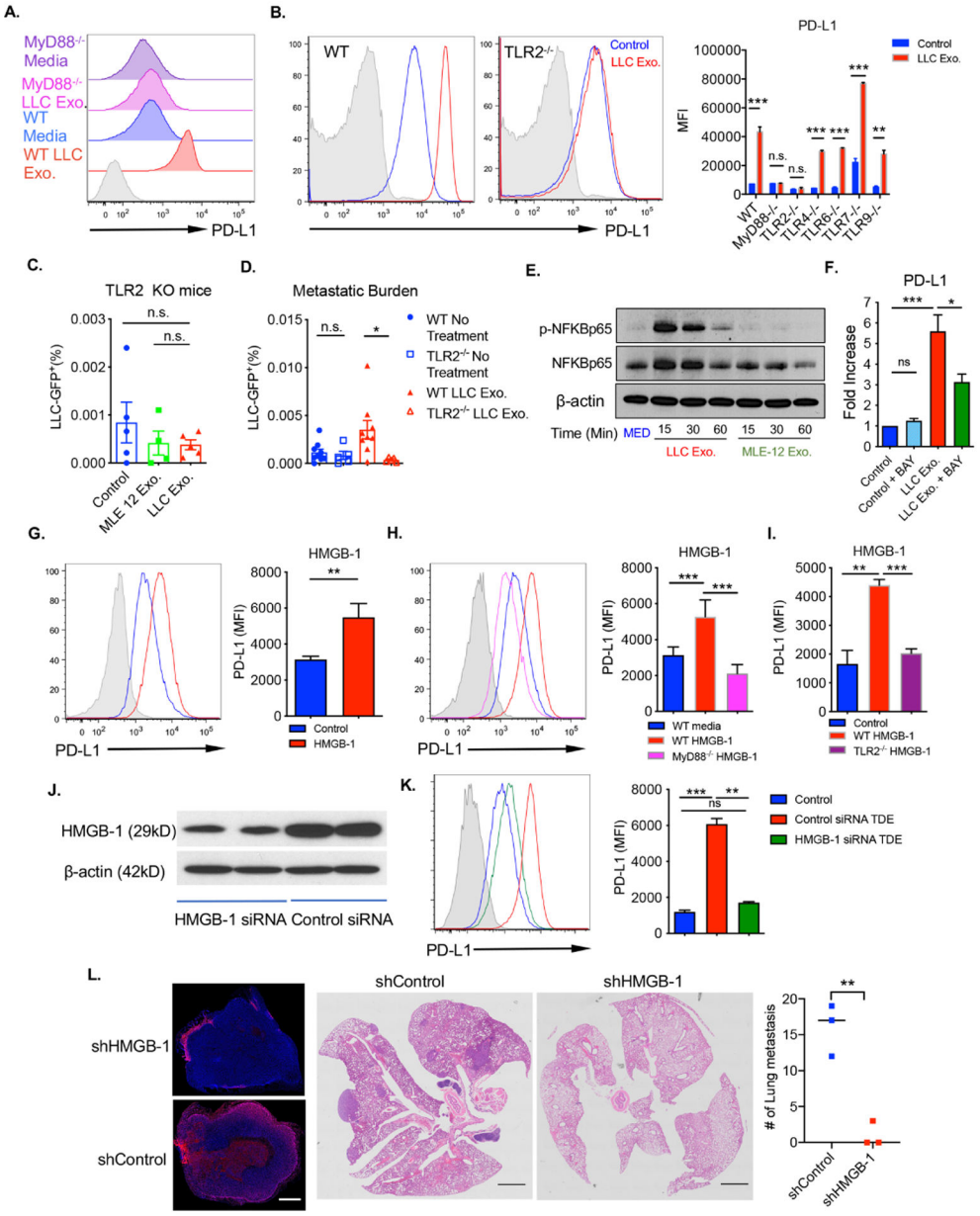


**Figure 3. TDE mediate PD-L1 expression through TLR2 and NF-κB.**

**(A)** The expression of PD-L1 by flow cytometry on WT or MyD88$^{-/-}$ peritoneal macrophages stimulated with LLC Exo.. **(B)** Expression of PD-L1 via flow cytometry in WT or TLR2$^{-/-}$ macrophages following stimulation with LLC Exo. (left). Macrophages from TLR4$^{-/-}$, TLR6$^{-/-}$, TLR7$^{-/-}$, and TLR9$^{-/-}$ mice (n=3) showed increased PD-L1 expression similar to WT following TDE stimulation (right). **(C)** Summary of GFP$^{+}$ micrometastases in the lungs of TLR2$^{-/-}$ mice that had previously been injected s.c. with GFP-LLC tumor cells and then treated i.v. with MLE-12 or LLC exosomes. Each dot represents data from one mouse. **(D)** Comparison of GFP$^{+}$ micrometastases between WT and TLR2$^{-/-}$ LLC Exo. treated mice. Each dot represents data from one mouse. **(E)** Activation of NF-κB signaling cascade in macrophages following stimulation with

MLE-12 or LLC Exo. at the indicated time determined by WB analysis. **(F)** PD-L1 mRNA expression level in macrophages pre-treated with the NF-κB inhibitor, BAY-11-7082 prior to stimulation with LLC Exo. Data was normalized to the control (n=3). **(G)** PD-L1 expression in macrophages stimulated with rmHMGB-1.
Representative histograms and summarized MFI data are shown (n=5). **p<0.01 (unpaired student's t test). **(H)** Comparison of PD-L1 expression between WT and MyD88$^{-/-}$ macrophages following stimulation with rmHMGB-1. Representative histograms and summarized MFI are shown (n=4). **(I)** PD-L1 expression in TLR2$^{-/-}$ macrophages compared to controls following rmHMGB-1 stimulation. Summarized MFI data is shown (n=3). **(J)** HMGB-1 expression in control siRNA or HMGB-1 siRNA transfected LLC cells assessed by Western blot. **(K)** PD-L1 expression on macrophages stimulated with TDE from control or HMGB-1 siRNA transfected LLC cells. Representative histogram and summarized data are shown (n=3). **(L)** Expression of HMGB-1 in either shControl or shHMGB-1 primary 4T1 s.c. tumors (left), H&E staining of lung (middle), and summarized number of metastatic tumor nodules (right) in the lungs. Scale bar=100μm. **p<0.01 (unpaired student's t test). The data are shown as mean ± SEM. *p<0.05, **p<0.01, ***p<0.001. See also Figure S3.

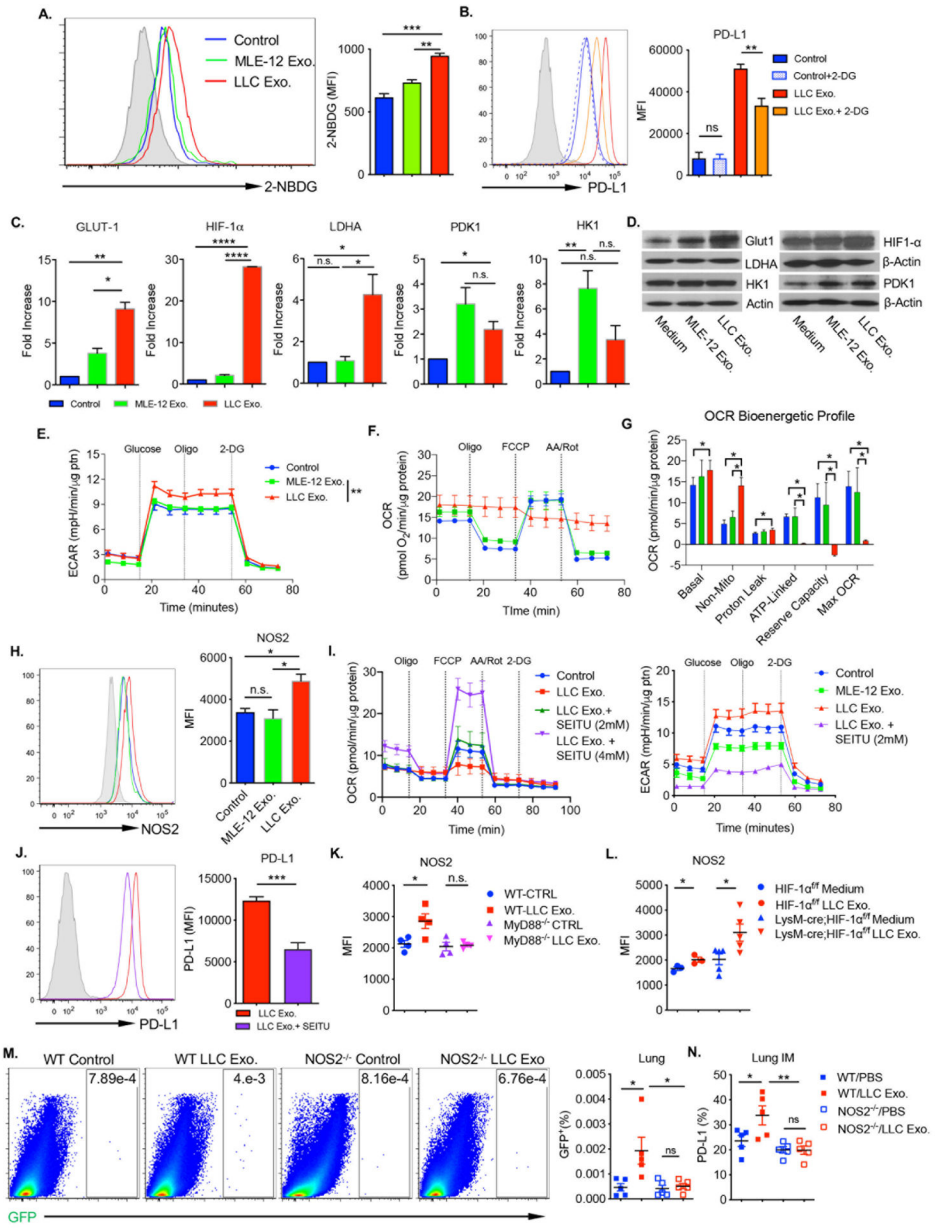


**Figure 4. TDE inhibit oxidative phosphorylation via NO.**

**(A)** Uptake of 2-NBDG in LLC or MLE-12 Exo. stimulated macrophages. Representative histograms and summarized data are shown (n=3). **(B)** PD-L1 expression on macrophages stimulated with LLC Exo. in the presence or absence of 1mM 2-DG. Representative histogram and summarized data are shown (n=3). **(C)** The mRNA expression levels of *GLUT-1*, *HIF-1α*, *LDHA*, *PDK1*, *HK-1*, and *IDH1* by RT-PCR in macrophages. Data normalized to control expression level (n=3). **(D)** Representative western blots showing expression of GLUT-1, LDHA, HK-1, HIF-1α and PDK1 in macrophages treated with MLE-12 Exo. or LLC Exo.. **(E)** Seahorse glycolysis stress test with sequential addition of glucose, oligomycin, and 2-DG in macrophages pre-treated with MLE-12 or LLC Exo. for 16 hours. Data are representative for n=4 independent experiments. **(F)** OCR measurement

in TDE stimulated macrophages. Data are representative of three independent experiments with similar results. **(G)** OCR Bioenergetic profiling showing relative values of parameters for representative Seahorse assay in Figure 4F. **(H)** Intracellular NOS2 expression via flow cytometry in macrophages stimulated with MLE-12 or LLC Exo.. Representative histogram and summarized data are shown (n=3). **(I)** OCR in macrophages treated with LLC Exo. in the presence of 2mM or 4mM SEITU (left). ECAR in the presence of SEITU (2mM) treated macrophages as measured by glycolysis stress test (right). Data are representative of two independent Seahorse Mito stress tests and two glycolytic stress test experiments each with similar results. **(J)** Expression of PD-L1 on macrophages treated with LLC Exo. in the presence or absence of SEITU (4mM). Representative histogram and summarized MFI data are shown (n=3). ***p<0.001 by unpaired student's t-test. **(K)** Intracellular NOS2 expression via flow cytometry in WT or MyD88$^{-/-}$ macrophages stimulated with LLC Exo.. n=4. **(L)** Intracellular NOS2 expression in HIF-1α$^{f/f}$ and LysM-cre;HIF-1α$^{f/f}$ macrophages upon LLC Exo. stimulation. **(M)** Micro-metastatic burden quantified by LLC-GFP% in the lungs of s.c. GFP-LLC tumor-bearing WT or NOS2$^{-/-}$ mice treated with LLC Exo. (n=5 mice per group). Representative dot plots and summarized data are shown. **(N)** PD-L1 expression on lung IMs of WT and NOS2$^{-/-}$ LLC Exo. treated mice (n=5 mice per group). The data are shown as mean ± SEM. *p<0.05, **p<0.01, ***p<0.00, ****p<0.0001 (one-way ANOVA with multiple comparisons). See also Figure S4.

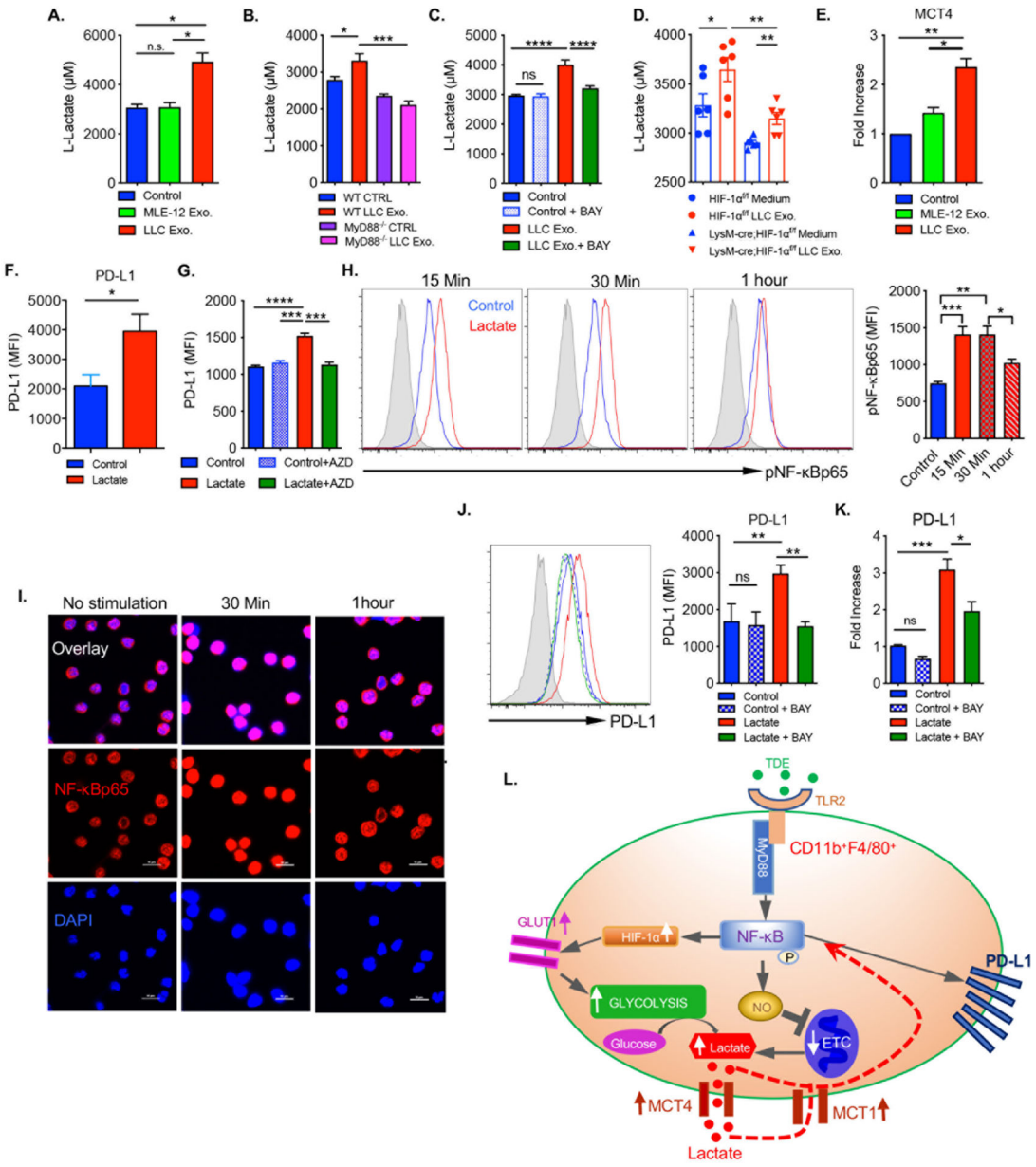


**Figure 5. Glycolytic metabolism fuels lactate production and PD-L1 expression.**

**(A)** Levels of L-lactate in the supernatants of macrophages treated with MLE-12 or LLC Exo. (n=3). **(B)** Level of L-lactate in the supernatant of WT or MyD88$^{-/-}$ macrophages stimulated with LLC Exo. (n=3). **(C)** L-lactate levels in the supernatant of macrophages pre-treated with BAY-11-7082 prior to stimulation with or without LLC Exo. (n=3). **(D)** Supernatants from HIF-1α$^{f/f}$ and LysM-cre;HIF-1α$^{f/f}$ peritoneal macrophages treated with LLC Exo. were collected and L-lactate concentration was determined (n=6). **(E)** The mRNA expression levels of *MCT-4* on macrophages treated with MLE-12 or LLC Exo. (n=3). Expression levels were normalized to the control. **(F)** Summarized PD-L1 expression via flow cytometry on macrophages stimulated with 20mM L-lactate (n=3). *p<0.05 (unpaired student's t test). **(G)** PD-L1 expression on macrophages treated with lactate in the presence

of the MCT-1 inhibitor AZD3965 (250nM) (n=3). **(H)** Intracellular phosphorylated NF-κBp65 (pNF-κBp65) expression following stimulation with L-Lactate for the indicated time. Representative histograms and summarized MFI data are shown (n=3). **(I)** Confocal translocation assay demonstrating increased co-localization of NF-κBp65 to the nucleus following 30 minutes stimulation with L-lactate. Scale bar=10μm. **(J)** PD-L1 expression on macrophages pretreated with BAY prior to stimulation with or without L-lactate. Representative histogram and summarized MFI data are shown (n=3). **(K)** mRNA levels of PD-L1 in macrophages pretreated with BAY prior to stimulation with or without L-lactate (n=4). **(L)** Schema depicting TDE-induced PD-L1 expression via direct NF-κB transcription and NF-κB mediated glycolytic metabolism. The data are shown as mean ± SEM. *p<0.05, **p<0.01, ***p<0.001, ****p<0.0001 (one-way ANOVA with multiple comparisons). See also Figure S5.

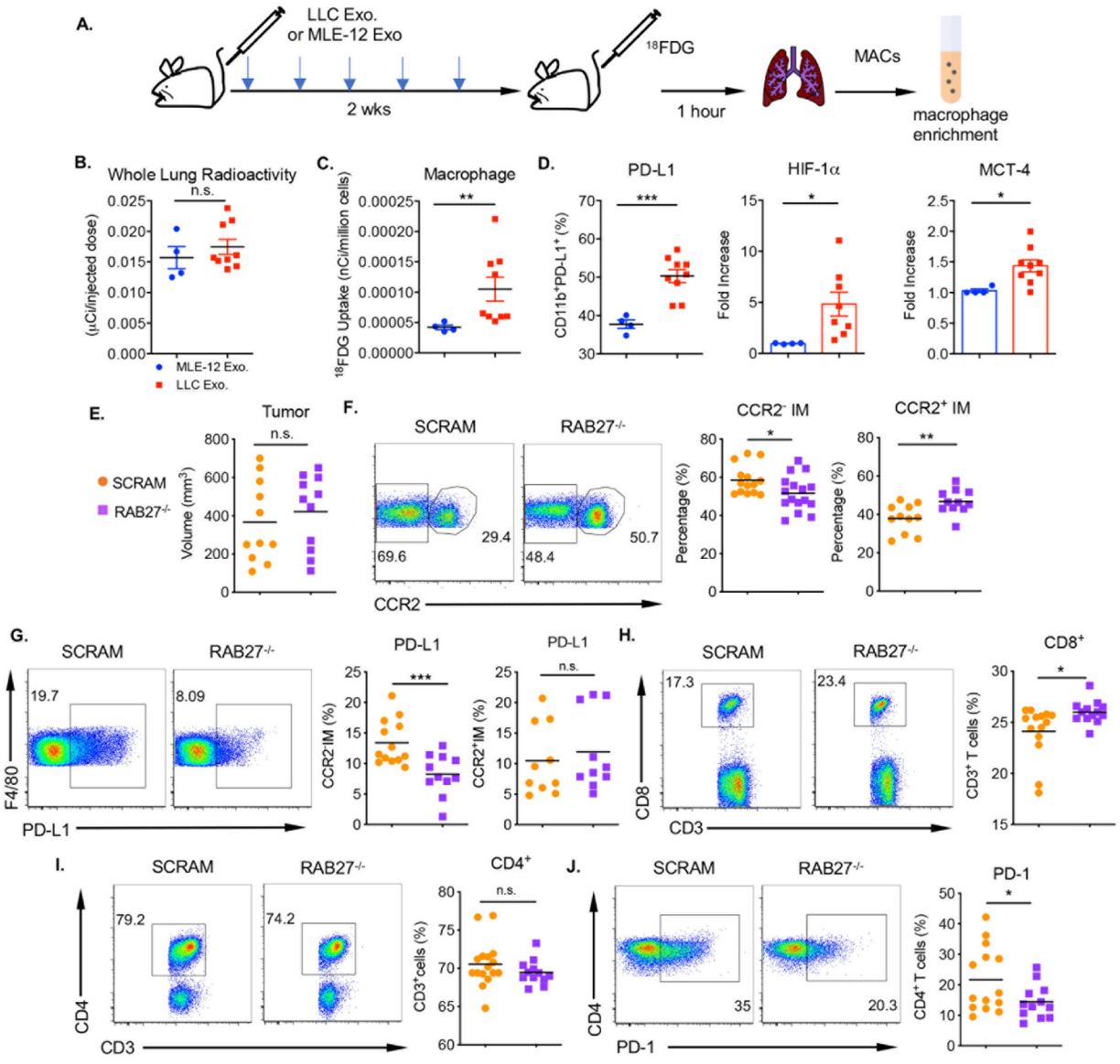


**Figure 6.** ***In vivo*** **assessment of TDE induced glycolytic and PD-L1 phenotype.**

**(A)** Schematic for experimental design (B-D). **(B)** Radioactivity measured by Biodex Atomlab™ 500 following intraperitoneal injection of $^{18}$FDG in the lungs of C57BL/6 mice treated with control MLE-12 Exo. or LLC Exo. Each dot represents data from one mouse. **(C)** $^{18}$FDG uptake in the macrophage enriched population from the lungs of MLE-12 Exo. or LLC Exo. treated mice. **p<0.01 via Mann-Whitney U test. **(D)** Flow cytometry expression of PD-L1 and mRNA expression of *HIF-1α* and *MCT-4* in the macrophage enriched population. **(E)** Primary tumor volume 28 days post injection with SCRAM or Rab27a$^{-/-}$ 4T-1 tumor cells. **(F-G)** CCR2 and PD-L1 expression on CD11b$^{+}$ IM in the lungs of SCRAM versus RAB27$^{-/-}$ tumor bearing mice. **(H)** Percentage of CD8$^{+}$ T cells in the lung. **(I-J)** Percentage and PD-1 expression of CD4$^{+}$ T cells in the lung. Representative dot plots and summarized data are shown. The data are shown as mean ± SEM. *p<0.05, **p<0.01, ***p<0.001 (unpaired student's t test). See also Figure S6.

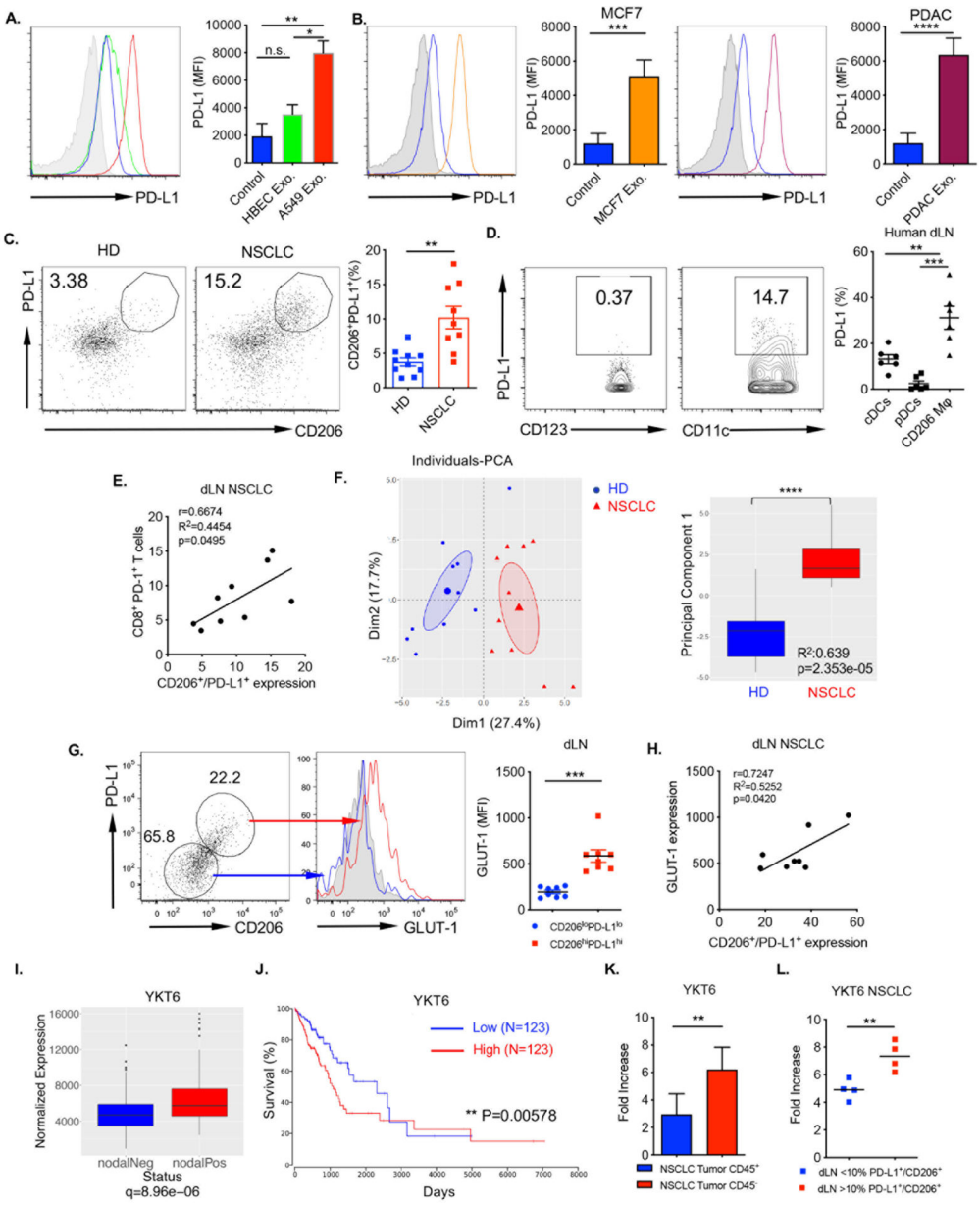


**Figure 7. The effect of human TDE on the formation of a pre-metastatic niche.**

**(A)** PD-L1 expression via flow cytometry on healthy donor sorted $CD14^+$ monocytes (n=3 donors) stimulated with control HBEC or A549 Exo.. Representative histogram and summarized data are shown. *p<0.05, **p<0.01, (one-way ANOVA with multiple comparisons). **(B)** PD-L1 expression on $CD14^+$ cells stimulated with exosomes from MCF-7 (left) or S2-013 (right). Representative histograms and summarized data are shown. n=3. ***p<0.001, ****p<0.0001 by unpaired student's t-test. **(C)** The expression of CD206 and PD-L1 on $CD68^+$ macrophages in the LNs of non-cancerous healthy donor (HD) lung transplants versus T1–3N0 NSCLC patients. **(D)** PD-L1 expression in $CD123^+$ pDCs and cDCs compared to $CD206^+$ macrophages in dLNs of NSCLC patients (n=6). Representative contour plots and summarized data are shown. **p<0.01, ***p<0.001 (one-way ANOVA

with multiple comparisons). **(E)** Pearson correlation between CD206/PD-L1$^{+}$ macrophages and CD8$^{+}$ PD-1$^{+}$ T cells within the dLN. **(F)** PCA plot of the first two principal components ("Dim1" and "Dim2"), depicting the relationships of NSCLC (red triangles) and HD (blue circles) subjects. The percent variance explained by each principal component is indicated in parentheses. The 95% confidence ellipses and centroids (enlarged symbols) for each group of samples (NSCLC and HD) are also shown (left). Boxplot depicting the values for the first principal component, partitioned by disease state (NSCLC vs. HD), as determined by PCA (right). ****p<0.0001 generated by linear regression. **(G)** GLUT-1 expression in CD206$^{hi}$PD-L1$^{hi}$ versus CD206$^{lo}$PD-L1$^{lo}$ CD68$^{+}$ macrophages obtained from dLN samples. Representative histograms and summarized data are shown. **(H)** Pearson correlation between CD206/PD-L1 and GLUT-1 expression in CD68$^{+}$ macrophages in NSCLC dLN. **(I)** Boxplot showing YKT6 expression in patients with negative nodal staging (N0) compared to positive nodal staging (N1-N3) in LUAD patients from the TCGA database. Plots were made with Deseq2's function plotCounts with count normalized to library size. Positive (N1-N3) n=85, Negative (NX/N0) n=156 **(J)** Kaplan-Meier survival curve generated by Oncolnc for TCGA dataset LUAD patients based on expression profile (High= top 25%) and (low=bottom 25%) of YKT6. n=123 per group. **p<0.01 (log rank test). **(K)** YKT6 mRNA expression levels in CD45$^{-}$ and CD45$^{+}$ cells sorted from primary NSCLC tumor samples. n=8. **(L)** YKT6 mRNA expression levels in NSCLC patient primary tumors grouped by CD206/PD-L1 expression level (high >10% CD68$^{+}$CD206$^{+}$PD-L$^{+}$ and low <10% CD68$^{+}$CD206$^{+}$PD-L$^{+}$ expression) in CD68$^{+}$ macrophages within the dLN. n=4 patients per group. The data are shown as mean ± SEM. **p<0.01, ***p<0.001 (unpaired student's t test). See also Figure S7.

## KEY RESOURCES TABLE

| REAGENT or RESOURCE | SOURCE | IDENTIFIER |
|---|---|---|
| **Antibodies** | | |
| Anti-Human CD68 PerCP-Cy5.5 (Clone Y1/82A) | Biolegend | Cat# 333813, RRID:AB_10681723 |
| Anti-Human PD-L1 (CD274) Pe-Cy7 (Clone 29E.2A3) | Biolegend | Cat# 329718, RRID:AB_2561687 |
| Anti-Human CD206 Brilliant Violet 421 (Clone 15-2) | Biolegend | Cat# 321126, RRID:AB_2563839 |
| Human Glut1 Mab (Clone 202915) antibody | R & D Systems | Cat# MAB1418, RRID:AB_2191039 |
| APC anti-human CD274 (B7-H1, PD-L1) antibody | Biolegend | Cat# 329707, RRID:AB_940358 |
| APC anti-mouse CD274 (B7-H1, PD-L1) antibody | Biolegend | Cat# 124312, RRID:AB_10612741 |
| Anti-Human CD11b Biotin (ICRF44) | Biolegend | Cat# 301304, RRID:AB_314156 |
| Anti-Human CD14 PE (HCD14) | Biolegend | Cat# 325606, RRID:AB_830679 |
| Anti-Human CD33 Brilliant Violet 605 (P67.6) | Biolegend | Cat# 366611, RRID:AB_2566404 |
| Anti-Human CD63 Brilliant Violet 650 (H5C6) | Biolegend | Cat# 353025, RRID:AB_2686995 |
| Anti-Human CD66b PE/Dazzle 594 (G10F5) | Biolegend | Cat# 305121, RRID:AB_2650717 |
| PE anti-mouse IFN-γ antibody | Biolegend | Cat# 505808, RRID:AB_315402 |
| PE anti-human IFN-γ (4S.B3) | Biolegend | Cat# 502509, RRID:AB_315234 |
| NOS2 (C-11) antibody | Santa Cruz | Cat# sc-7271, RRID:AB_627810 |
| Phospho-NF-κB (Ser536) (E1ZIT) | Cell Signaling Technology | Cat# 13346, RRID:AB_2798185 |
| NF-κB p65 (D14E12) XP Rabbit mAb | Cell Signaling Technology | Cat# 8242 |
| Alexa Fluor 555 Donkey anti-rabbit IgG antibody | Biolegend | Cat# 406412, RRID:AB_2563181 |
| Goat Anti-Mouse B7-h1/ PD-L1 Polyclonal Antibody, Unconjugated | R and D Systems | Cat# AF1019, RRID:AB_354540 |
| Monoclonal Anti-β-Actin Clone AC-74 | Sigma | Cat# A5316 |
| HMGB1 (D3E5) Rabbit mAb | Cell Signaling Technology | Cat# 6893S, RRID:AB_10827882 |
| Anti-Human CD45 (HI30)-89Y | Fluidigm | Cat#3089003B |
| Purified anti-human CD14 (Maxpar® Ready) Antibody | Biolegend | Cat#301843, RRID:AB_2562813 |
| Purified anti-human CD11b (Maxpar® Read) Antibody | Biolegend | Cat#301337, RRID:AB_2562811 |
| Anti-Human CD11c (Bu15)-147Sm | Fluidigm | Cat#3147008B |
| Anti-Human CD274/PD-L1 (29E.2A3)-175Lu | Fluidigm | Cat#3175017B |
| Anti-Human CD206/MMR (15-2)-168Er | Fluidigm | Cat#3168008B |
| Anti-Human CD123/IL-3R (6H6)-143Nd | Fluidigm | Cat#3143014B |
| Glut1 (D3J3A) Rabbit mAb | Cell Signaling Technology | Cat#12939, RRID:AB_2687899 |
| LDHA Antibody | Cell Signaling Technology | Cat#2012, RRID:AB_2137173 |
| Mouse Anti-Rab 27a Monoclonal Antibody (E-8) | Santa Cruz | Cat#sc-74586, RRID:AB_2176724 |
| CD3 Monoclonal Antibody (OKT3) | Thermo Fisher Scientific | Cat#16-0037-81 |
| CD282 (TLR2) Antibody (TL2.1) | Thermo Fisher Scientific | Cat#16-9922-82 |
| Flotillin-1 (D2V7J) XP ® Rabbit mAb | Cell Signaling Technology | Cat#18634 RRID:AB_2773040 |
| HMGB1 (D3E5) Rabbit mAb | Cell Signaling Technology | Cat#6893 RRID:AB_10827882 |
| HSP70 (D69) Antibody | Cell Signaling Technology | Cat#4876 RRID:AB_2119693 |
| Alix (3A9) Mouse mAb | Cell Signaling Technology | Cat#2171 RRID:AB_2299455 |

| REAGENT or RESOURCE | SOURCE | IDENTIFIER |
|---|---|---|
| Annexin V Antibody | Cell Signaling Technology | Cat#8555 RRID:AB_10950499 |
| Human YKT6 antibody | Bethtl Laboratories | Cat# A305-480A |
| Human β actin antibody | Sigma | Cat# A5316 |
| **Bacterial and Virus Strains** | | |
| NEB 5-alpha Competent *E.coli* cells | New England Biolabs | Cat# C2987I |
| | | |
| **Biological Samples** | | |
| Cadaveric lymph node samples | University of Louisville Health | N/A |
| NSCLC draining lymph node samples | University of Louisville Health | N/A |
| NSCLC lung tissue samples | University of Louisville Health | N/A |
| PBMC from healthy donors | University of Louisville Health | N/A |
| **Chemicals, Peptides, and Recombinant Proteins** | | |
| Phorbol 12-myristate 13-acetate, approx. 99% | Sigma | |
| Brefeldin A Solution | Biolegend | Cat# 420601 |
| Streptavidin MicroBeads | Miltenyi Biotec | Cat# 130-048-101 |
| CD8a (ly-2) MicroBeads | Miltenyi Biotec | Cat# 130-049-401 |
| CD4 (L3T4) MicroBeads | Miltenyi Biotec | Cat# 130-049-201 |
| BODIPY FL Maleimide | Invitrogen | Cat# B10250 |
| S-Ethylisothiourea HBr | Enzo Life Sciences | Cat# ALX-270-025-M250 |
| BAY 11-7082 | Sigma | Cat# B5556 |
| AZD3965 | MedChemExpress | Cat# HY-12750 |
| Recombinant Mouse HMGB-1 | Biolegend | Cat# 764006 |
| Recombinant Human HMGB1 Protein | R & D Systems | Cat# 1690-HMB-050 |
| Actinomycin D | Gibco | Cat# 50-76-0 |
| Sodium L-lactate | Sigma | Cat# L7022-5G |
| Dimethyl 2-oxoglutarate | Sigma | Cat# 349631 |
| $H_2$DCFDA | Invitrogen | Cat# D399 |
| Linoleic Acid | Sigma | Cat# L1376 |
| BD GolgiStop | BD Bioscience | Cat# 51-2092KZ |
| Intracellular Staining Perm Wash Buffer | Biolegend | Cat# 421002 |
| Fixation Buffer | Biolegend | Cat# 420801 |
| eBioscience FOXP3/Transcription | Invitrogen | Cat# 00-5523-00 |
| Poly-L-Lysine Solution | Sigma Aldrich | Cat# P4832 |
| Lipofectamine 2000 Reagent | Thermo Fisher Scientific | Cat# 11668-019 |
| Gibco Opti-MEM I Reduced Serum Media | Thermo Fisher Scientific | Cat# 31985070 |
| Lipopolysaccharides from *Escherichia coli* O111:B4 | Sigma | Cat# L4391 |
| CpG ODN 1668 | InvivoGen | Cat# tlrl-1668 |
| CL075 | InvivoGen | Cat# tlrl-c75 |
| Kanamycin | Sigma | Cat# K1876-1G |
| Lennox LB microbial growth medium | Sigma | Cat# L3022 |

| REAGENT or RESOURCE | SOURCE | IDENTIFIER |
|---|---|---|
| SOC outgrowth medium | New England Biolabs | Cat# B9020S |
| **Critical Commercial Assay** | | |
| Exo-Check Exosome Antibody Arrays | System Biosciences | Cat# EXORAY200A-4 |
| L-Lactate Assay Kit I | Eton Bioscience | Cat# 120001100P |
| Seahorse XF Glycolysis Stress Test Kit | Agilent Technologies | Cat# 103020-100 |
| ELISA MAX Standard Set Mouse IL-6 | Biolegend | Cat# 431303 |
| ELISA MAX Standard Set Mouse IL-10 | Biolegend | Cat# 431411 |
| ELISA MAX Standard Set Mouse TNF-α | Biolegend | Cat# 430901 |
| ToxinSenor Single Test Kit Sensitivity 0.25 EU/mL | GenScript | Cat# L00451-40 |
| Mouse Cytokine Array Kit Panel A | R and D Systems | Cat# ARY006 |
| CellTrace CFSE Cell Proliferation Kit | Invitrogen | Cat# C34554 |
| Universal Mycoplasma Detection Kit | ATCC | Cat# 30-1012K |
| Mouse ALB ELISA Kit | Biorbyt | Cat# orb437837 |
| Mouse HDL ELISA Kit | Biorbyt | Cat# orb548990 |
| Mouse LDL ELISA Kit | Biorbyt | Cat# orb553688 |
| Endotoxin Free Plasmid Maxi Kit | Qiagen | Cat# 12362 |
| Deposited Data | | |
| | | |
| | | |
| | | |
| | | |
| | | |
| **Experimental Models: Cell Lines** | | |
| LL/2 (LLC1) | ATCC | Cat#CRL-1642 |
| Mouse Lung epithelial-12 | ATCC | Cat#CRL-2110 |
| A549 human lung adenocarcinoma | ATCC | Cat#CCL-185 |
| Primary Bronchial/Tracheal Epithelial Cells; Normal, Human | ATCC | Cat#PCS-300-010 |
| 4T-1 murine breast carcinoma | ATCC | Cat#CRL-2539 |
| Pan02 murine pancreatic adenocarcinoma | The laboratory of Dr. Yong Lu | N/A |
| MC38 murine colon carcinoma | kerafast | Cat#ENH204-FP |
| B16-F10 murine melanoma | ATCC | Cat#CRL-6475 |
| MCF7 human breast carcinoma | ATCC | Cat#HTB-22 |
| S2-013 human pancreatic ductal adenocarcinoma | The laboratory of Dr. Robert Martin | N/A |
| **Experimental Models: Organisms/Strains** | | |
| C57BL/6 | The Jackson Laboratory | Stock#000664 |
| BALB/cJ | The Jackson Laboratory | Stock#000651 |
| B6.129P2-NOS2$^{tm1Lau}$/J | The Jackson Laboratory | Stock#002609 |
| C57BL/6-tg(TcraTcrb)1100Mjb/J | The Jackson Laboratory | Stock#003831 |
| B6.Cg-Tg(TcraTcrb)425Cbn/J | The Jackson Laboratory | Stock#004194 |
| B6.129P2(SJL)-Myd88$^{tm1.1Defr}$/J | The Jackson Laboratory | Stock#009088 |
| B6.129-Tlr2$^{tm1Kir}$/J | The Jackson Laboratory | Stock#004650 |

| REAGENT or RESOURCE | SOURCE | IDENTIFIER |
|---|---|---|
| B6(Cg)-Tlr4$^{tm1.2Karp}$/J | The Jackson Laboratory | Stock#029015 |
| TLR6$^{-/-}$ | 3M Pharmaceuticals | N/A |
| TLR7$^{-/-}$ | 3M Pharmaceuticals | N/A |
| TLR9$^{-/-}$ | Oriental Yeast Co., Japan | N/A |
| B6.129-Hif1a$^{tm3Rsjo}$/J | The Jackson Laboratory | Stock#007561 |
| B6.129P2-Lyz2$^{tm1(cre)Ifo}$/J | The Jackson Laboratory | Stock#004781 |
| **Oligonucleotides** | | |
| Rab27a sgRNA CRISPR All-in-One Lentivirus (Mouse) | abm | Cat#K3783417 |
| Scrambled sgRNA CRISPR/Cas9 All-in-One Lentivirus | abm | Cat#K011 |
| See Supplemental Table S2 for oligonucleotide sequences used for real-time quantitative PCR | This paper | N/A |
| MISSION esiRNA targeting mouse HMGB1 | Sigma Aldrich | Cat#EMU210181 |
| MISSION esiRNA targeting eGFP | Sigma Aldrich | Cat#EHUEGFP |
| | | |
| **Recombinant DNA** | | |
| C1-eGFP-huYKT6, YKT6 V-SNARE Homolog (YKT6; NM_006555): Human Tagged Clone (N-terminal eGFP-tagged) subcloned into C1-eGFP; Predicted Masses: 22,418 Da for YKT6, 26,870 Da for GFP, and 49,288 Da (or 49.3 kDa) for the fusion protein (McGrath et al. 2021) | The laboratory of Dr. Gabriela Caraveo Piso | N/A |
| C1-eGFP, mammalian vector, Predicted Mass: 26,870 Da, or 26.9 kDa GFP (McGrath et al. 2021) | Dr. Gabriela Caraveo Piso | N/A |
| | | |
| | | |
| **Software and Algorithms** | | |
| FlowJo v.10 | BD | https://www.flowjo.com/ |
| ImageJ | NIH | https://imagej.nih.gov/ij |
| GraphPad Prism | GraphPad Software | https://www.graphpad.com/scientific-software/prism/ |
| CyTOF Software v7.0 | Fluidigm | https://www.fluidigm.com/software |
| Seahorse Wave Controller software | Seahorse/Agilent | https://www.agilent.com/en/product/cell-analysis/real-time-cell-metabolic-analysis/xf-software/seahorse-wave-controller-software-2-4-2-740903 |
| **Metabolites** | | |
| See Table S3 for LC-MS mediated determination of metabolites. | This paper | N/A |
| | | |
| | | |
| | | |
| | | |